NUMERICAL MODELING OF DISPERSE MATERIAL EVAPORATION IN AXISYMMETRIC THERMAL PLASMA REACTOR

by

Predrag STEFANOVIĆ, Dejan CVETINOVIĆ, Goran ŽIVKOVIĆ, Simeon OKA, and Pavle PAVLOVIĆ

A numerical 3D Euler-Lagrangian stochastic-deterministic (LS(D) model of two-phase flow laden with solid particles was developed. The model includes the relevant physical effects, namely phase interaction, particle dispersion by turbulence, lift forces, particle-particle collisions, particle-wall collisions, heat and mass transfer between phases, melting and evaporation of particles, vapour diffusion in the gas flow. It was applied to simulate the processes in thermal plasma reactors, designed for the production of the ceramic powders. Paper presents results of extensive numerical simulation provided (a) to determine critical mechanism of interphase heat and mass transfer in plasma flows, (b) to show relative influence of some plasma reactor parameters on solid precursor evaporation efficiency: 1 – inlet plasma temperature, 2 – inlet plasma velocity, 3 – particle initial diameter, 4 – particle injection angle ά, and 5 – reactor wall temperature, (c) to analyze the possibilities for high evaporation efficiency of different starting solid precursors (Si, Al, Ti, and B_2O_3 powder), and (d) to compare different plasma reactor configurations in conjunction with disperse material evaporation efficiency.

Key words: two-phase flow, thermal plasma, heat and mass transfer, turbulence, solid particles evaporation, ceramic powders synthesis, numerical modeling

Introduction

For thermal plasma processing of solid particles (including processes like plasma spraying, spheroidizing, decomposition, melting or fuming of fine particles, synthesis of ultrafine particles, *etc.*) injection and mixing, *i. e.* momentum, heat and mass transfer between solid particles and plasma flow is of great importance for the quality of the product. This is especially pronounced in plasma processes for the gas phase synthesis of pure, ultrafine ceramic powders like: Si_3N_4, SiC, AlN, TiN, BN, *etc.*, where solid particles are used as a precursor. Thermodynamic studies of high temperature

chemical equilibria of the Si-N system 1 and published experimental data on plasma synthesis of ultrafine silicon nitride powder 2-4 undoubtedly show the importance of total evaporation of the injected silicon particles in plasma reactor for the purity *i. e.* quality of obtained powder. Namely, if evaporation is not complete, the remaining particles become seeds which foster early nucleation and condensation of unwanted silicon droplets at high temperatures (T < 3000 K) instead of synthesis of silicon nitride particles at lower temperatures (T < 1900 K) during the quenching process. In plasma synthesis of other nitride or carbide ultrafine powders for obtaining pure product it is also essential to completely evaporate starting (metal or oxide) powder precursor.

There are numerous effects involved in plasma-solid particle interaction which have great influence on interphase heat and mass transfer *i. e.* on evaporation process. On the other hand, due to the difficulties in experimental investigations of two-phase high temperature flows, there is a lack of corresponding experimental data. So, numerical modeling of two phase plasma flows and few rather simple diagnostic methods are in most cases, the main tools for developing and optimizing the plasma reactors and processes. This work is the result of the extensive numerical simulation which have been conducted:

– to determine critical mechanism of interphase heat and mass transfer in plasma flows,
– to show relative influence of some plasma reactor parameters on solid precursor evaporation efficiency: inlet plasma temperature, inlet plasma velocity, particle initial diameter, particle injection angle α, and reactor wall temperature,
– to analyze the possibilities for high evaporation efficiency of different starting solid precursors (Si, Al, Ti and B_2O_3 powder), and
– to compare different plasma reactor configurations in conjunction with disperse material evaporation efficiency.

For this purpose a full 3D two phase gas-dispersed particles model was developed. It was in the first stage developed as a general model, suitable for use in numerous fields of application, and then it was implemented and adjusted for simulation of thermal plasma processes.

Flows with a dispersed phase in a continuum are influenced by the interaction between the phases. Contrary to the continuous phase where information about local characteristics of the fluid is transported by the molecular interaction through pressure waves and diffusion, in the dispersed phase there is no analogy for the fluid pressure, and information is transported between bubbles or particles through the conveying fluid. Due to their different histories, there are local differences between hydrodynamic properties of bubbles and solid particles, which is not the case for the continuous phase. There are also phenomena in the dispersed phase with the characteristics of diffusion, caused mainly by the turbulent fluctuations in the continuous phase.

Mathematical treatment of multidimensional multiphase flows for simulating these phenomena is complicated and not yet solved. The exact approach for modelling

convection and diffusion processes in multiphase flows requires the knowledge of turbulent characteristics as fluctuation velocity components, autocorrelation functions and Lagrangian integral scales of turbulence. These characteristics are not known for multiphase flows even in the simplest cases. That is why the only possible practical approach is to develop physical and mathematical models closing the problem by using assumptions on the characteristics of the involved phenomena, or by introducing empirical correlations. Enhanced physical knowledge is required to develop improved multiphase models. It is a big challenge to overcome the closure problems between the flow equations of the different phases. Many details about forces on the phases and their interaction are still unknown. There is also a lack of knowledge about the influence of the dispersed phases on the turbulent velocity fluctuations in the continuous phase which is necessary for improving turbulence models. To obtain insight into details of the flow, *e. g.* the slip velocity or the wall shear stress, the separate measurement of local flow properties of the different phases is essential.

For modeling the dispersed phase, either the Eulerian or the Lagrangian approach can be used. The Eulerian approach treats the dispersed phase like a fluid. Its main advantage is that it is less time consuming on the computer than the Lagrangian approach. An example of successful two-phase flow modeling by the Eulerian approach is the work of 5 . The Lagrangian approach is closer to the physical reality and yields information necessary for an accurate prediction of particle motion in the turbulent field. For this reason it has been chosen for the present work.

The theoretical basis for phase interaction was established by 6 . According to their model, solid particles, drops and bubbles are treated as sources of mass, momentum and energy in the fluid, represented by source terms in the equations of change. Crowe *et al*. 7 used this idea to develop the Particle-Source-in-Cell (PSI-CELL) model. In many models developed later, special attention was given to some particular phenomena in multiphase flows. Rubinow and Keller 8 developed a theoretical expression for the lift force which acts on a sphere rotating in a viscous fluid. Saffman 9 modeled the motion of a sphere near the wall, where the influence of the fluid velocity gradient on the sphere motion was taken into account. Matsumoto and Saito 10 modelled particle-wall collisions and investigated the role of wall roughness in preventing particle sedimentation. Wall roughness was modelled by a periodic sinusoidal function, with its amplitude representing the roughness height. Particle non-sphericity was accounted for by treating the particles as ellipsoids. Tsuji *et al.* 11 developed a two-phase model for the flow through a horizontal tube, taking into account the Magnus lift force. Milojević 12 modelled the effect of fluid turbulence on the dispersed phase, taking into account the crossing-trajectories effect. Sommerfeld and Živković 13 , similar to 14 , developed a model in which they simulated wall roughness by the stochastic change of the wall inclination in the model. They also developed a model for particle-particle collisions. The collisions were regarded as a stochastic event, similar to collisions between gas molecules, which can be described by the kinetic theory of gases.

Mathematical model of multiphase flow and
heat and mass transfer between phases

Mathematical model for simulating steady multiphase flows was developed. The hot gas was treated following the Eulerian approach, *i. e.* its parameters were defined as functions of spatial coordinates. Solid particles and droplets were treated following the Lagrangian approach, which means that the parameters of every particle or droplet are functions of time 15 . Even though this means that in the equations of particle motion time appears explicitly, the mean characteristics of the dispersed phase in a sufficiently long period of time do not change, so that we can consider them as stationary. As results of this computation, one obtains the fields of mean velocities, turbulent kinetic energy and dissipation rate, temperature, concentration, pressure drop, and mean velocities, mean diameter and mass concentration for the dispersed phase.

Equations of fluid motion

The motion of the fluid is described by the continuity and the Navier-Stokes equations. Turbulence is modelled by the standard *k*-model 16, 17 . The equations for the liquid flow are

$$\frac{\partial(\rho U_i)}{\partial x_i} \quad 0 \qquad \qquad \text{(Continuaty)} \qquad (1)$$

$$\frac{\partial}{\partial x_j} \quad \rho U_i U_j \quad \overline{\rho u_i u_j} \quad \mu \frac{\partial U_i}{\partial x_j} \qquad \frac{\partial P}{\partial x_i} \quad S_{u_i}^P \qquad \text{(Navier-Stokers)} \qquad (2)$$

$$\frac{\partial}{\partial x_j} \quad \rho U_j k \quad \frac{\mu_{\text{eff}}}{\sigma_k} \frac{\partial k}{\partial x_j} \qquad P_k \quad \rho \varepsilon \quad S_k^P \qquad \text{(Turbulent kinetic energy)} (3)$$

$$\frac{\partial}{\partial x_j} \quad \rho U_j \varepsilon \quad \frac{\mu_{\text{eff}}}{\sigma_\varepsilon} \frac{\partial \varepsilon}{\partial x_j} \qquad \frac{\varepsilon}{k}(C_{\varepsilon 1} P_k \quad C_{\varepsilon 2} \rho \varepsilon) \quad S_\varepsilon^P \qquad \text{(Turbulent dissipation)} \quad (4)$$

$$\frac{\partial}{\partial x_j} \quad \rho U_j h \quad \frac{\mu_{\text{eff}}}{\sigma_h} \frac{\partial h}{\partial x_j} \qquad S_R \quad S_h^P \qquad \text{(Energy equation)} \qquad (5)$$

$$\frac{\partial}{\partial x_j} \quad \rho U_j m_v \quad \frac{\mu_{\text{eff}}}{\sigma_m} \frac{\partial m_v}{\partial x_j} \qquad S_m^P \qquad \text{(Vapor conservation)} \qquad (6)$$

$$\mu_{\text{eff}} \quad \mu \quad \mu_t \qquad \mu_t \quad \frac{C_\mu \rho k^2}{\varepsilon} \qquad P_k \quad \mu_{\text{eff}} \frac{\partial U_i}{\partial x_j} \quad \frac{\partial U_j}{\partial x_i} \quad \frac{\partial U_i}{\partial x_j}$$

66

In these equations U_i denotes the cartesian velocity components, x_i cartesian co-ordinates, P the fluid pressure, k and ε turbulent kinetic energy and dissipation rate, ρ and μ the fluid density and dynamic viscosity, and μ_t the turbulent viscosity. Source terms due to the presence of particles are denoted by the superscript p and are given according to [18] by the equations

$$S_{u_i}^p = \frac{1}{V_{cv} t_{tot}} \sum_n m_n (U_i^{out} - U_i^{in} - g_i \Delta t_{cv})$$
$$S_k^p = \sum_i \overline{u_i S_{u_i}^p} - \overline{u_i} \overline{S_{u_i}^p} \qquad (7)$$
$$S_\varepsilon^p = C_3 \frac{\varepsilon}{k} S_k^p$$

Here V_{cv} is the control volume, t_{tot} the total time period covered by the calculation of n parcels, m_n the mass of a parcel, and Δt_{cv} the total time of a parcel spent in the control volume.

The term parcel will be discussed in Section 3.3. The summation is performed over all particles passing the considered control volume in the period t_{tot}. For the k-ε model and heat transfer models, the following standard coefficients are used:

C_μ	$C_{\varepsilon 1}$	$C_{\varepsilon 2}$	C_3	σ_k	σ_ε	s_m	σ_h
0.09	1.44	1.92	0.7	1.0	1.3	0.9	0.9

The dependent variable in the energy equation is the enthalpy of gas mixture – h, which includes vapor evaporation heat: $h = m_g h_g + m_v h_v + m_v H_v$, where $m_g + m_v = 1$ are the mass fractions of plasma gas and vapor, and T_g is the local plasma gas mixture temperature.

The source term S_R in eq. (5) is the volumetric source of energy due to radiation, computed by the six-flux model of De Marco and Lockwood. For axisymmetric flow this model yields two equations for mean radiative fluxes in axial and radial directions:

$$\frac{\partial}{\partial x}\left(\frac{1}{K_{at}}\frac{\partial F_x}{\partial x}\right) - \frac{4}{3}K_{at}(F_r - 2F_x) + \frac{4}{3}\sigma(K_{ag}T_g^4 - K_{ap}T_p^4) = 0 \qquad (8)$$

$$\frac{1}{r}\frac{\partial}{\partial r}\left(\frac{1}{K_{at}}r\frac{\partial F_r}{\partial x}\right) - \frac{4}{3}K_{at}(F_x - 2F_r) + \frac{4}{3}\sigma(K_{ag}T_g^4 - K_{ap}T_p^4) = 0 \qquad (9)$$

which should be solved numerically too. In these equations $K_{at} = K_{ag} + K_{ap}$ is total absorption coefficient defined per unit length as a sum of gas (K_{ag}) and particle (K_{ap}) absorption coefficient, $\sigma = 5.76 \cdot 10^{-8}$ W/m²K⁴ is the black body radiation constant and T_p is the particle temperature.

Equation (8) and (9) are connected with the first six conservation equations through the coefficients and the radiation source term in the energy conservation equation, defined as:

$$S_R \frac{16}{9} K_{at}(F_x \quad F_r) \quad \frac{32}{9} K_{ag} \sigma T_g^4 \quad \frac{32}{9} K_{ap} \sigma T_p^4 \qquad (10)$$

For solving this system of equations, the control volume method was adopted. The basis of the code was the numerical code CAST for single-phase flow, based on the SIMPLE algorithm, with collocated grid and hybrid scheme. This code was extended by introducing the additional source terms eq. (7) to account for the presence of particles.

The solution the above set of equations was subject to the boundary conditions at the entrance of plasma reactor – profile of the flow velocity U_x uniform with the value to represent the flow rate, $U_y = U_z = 0$, and turbulence level based on U_x assumed to be 10% – and at the reactor walls – logarithmic wall functions used to calculate the flow velocity in x direction at the grid level closest to the wall, while representing the wall shear stress correctly. The outflow level was placed far enough downstream to ensure vanishing gradients of the flow parameters in flow direction.

Equations of motion of particles and droplets

For describing the particle and drop motion correctly, all significant forces acting during the motion must be taken into account. There are two kinds of such forces – those acting permanently, and those acting as impulses [14, 19, 20]. The origin of the first kind of forces is the presence of the continuous liquid phase and gravity, while the second kind of forces is caused by particle-wall and particle-particle interactions.

For proper calculation of a force acting on some body, it is necessary to know the body shape. In principle the shape of both solid particles and drops is irregular. Accordingly, there are some models of particle motion, which take into account the shape of the particles 21 . In a wide range of other models, however, particles and drops are treated as spheres. The most important force is the drag force, which is defined by the equation

$$\vec{F}_D \quad C_D \frac{\pi d_p^2}{4} \frac{1}{2} \rho(\vec{U} \quad \vec{V})|\vec{U} \quad \vec{V}| \qquad (11)$$

Here we denote the particle properties with subscript p to mean both drops and solid particles. The drag coefficient C_D depends on the particle Reynolds number $\mathrm{Re}_p \quad d_p \rho |\vec{U} \quad \vec{V}| / \mu$, with the particle size d_p. Among many expressions for C_D which can be found in the literature, in the calculations were used expressions as explained in Section 2.3.

Due to frequent collisions with the walls, the particles can rotate with large angular velocity $\vec{\omega}_p$. In a viscous fluid this rotation induces a lift force and torque, which have to be taken into account in the calculation of the solid particle or droplet motion.

Rubinow and Keller [8] analysed the rotation of a sphere in a viscous fluid with small particle Reynolds number and obtained the following relation for the lift force and torque:

$$\vec{F}_L = \pi \frac{D_p^3}{8} \rho \vec{\omega}_p \times \vec{U}[1 - G(\text{Re}_p)] \tag{12}$$

$$\vec{T} = \pi \mu D_p^3 \vec{\omega}_p [1 - g(\text{Re}_p)] \tag{13}$$

where $G(\text{Re}_p)$ and $g(\text{Re}_p)$ are functions of the particle Reynolds number. Rubinow and Keller [8] proved that, for small Reynolds numbers, these functions could be neglected. They also showed that particle rotation does not influence the drag force and vice versa, so that these effects can be treated separately. In the case of turbulent flow, the rotation of the fluid should also be accounted for. According to [19], this can be done by introducing the additional term $\frac{1}{2} \nabla \times \vec{U}$ into eqs. (12) and (13), to obtain:

$$\vec{F}_L = \pi \frac{D_p^3}{8} \rho \left(\vec{\omega}_p - \frac{1}{2} \nabla \times \vec{U} \right) \times (\vec{V} - \vec{U}) \tag{14}$$

$$\vec{T} = \pi \mu D_p^3 \left(\vec{\omega}_p - \frac{1}{2} \nabla \times \vec{U} \right) \tag{15}$$

If there is a velocity gradient in the fluid through which the particle moves, the pressure field around the particle is no more symmetrical, and the resulting drag force deviates from eq. (14). This effect can be explained by the action of a new force (with the drag force remaining the same as before). This new force was analyzed by [9], for the case of particle motion through a very viscous fluid, and for the case of a velocity gradient perpendicular to the direction of motion. The value of the force is relatively small in many cases, but it can be important for small particles in the near-wall regions, where the fluid velocity gradient is high. Saffman derived the force only for two-dimensional motion (particle velocity and velocity gradient in one plane). Živković [22] developed a generalization of the expression of the Saffman force for the three-dimensional case, which reads

$$\vec{F}_S = 1.54 m_p \frac{(\rho \mu)^{1/2}}{\rho_p d_p \left\| \nabla \times (\vec{V} - \vec{U}) \right\|^{1/2}} \nabla \times (\vec{V} - \vec{U})^2 \tag{16}$$

with the particle mass m_p. Gravitational and buoyancy forces are included by the equation

$$\vec{F}_B = V_p(\rho_p - \rho)\vec{g} \tag{17}$$

where V_p is the particle volume. Besides the above mentioned forces, there are also forces due to the pressure gradient, so called "additional mass" force due to the local acceleration of the fluid, which leads to an additional resistance of the fluid against the particle motion, as well as the Basset force. These three terms, however, can be

neglected in the present case of steady flow with small differences between particle and fluid velocities.

For solving the equations of particle motion, a semi-analytical approach was adopted. For realizing this approach, the whole time interval during which the particle was followed was divided into subintervals. Particle position, velocity and angular velocity, particle diameter and temperature were calculated at the end of each subinterval. Regarding the forces as constant during one subinterval, the differential equations for particle motion read:

$$\frac{d\vec{V}}{dt} = \frac{\pi d_p \mu C_D \, \mathrm{Re}_p}{8 m_p}(\vec{U} - \vec{V}) + \vec{g}\left(1 - \frac{\rho}{\rho_p}\right) + \frac{\vec{F}_L + \vec{F}_S + \vec{F}_{AM}}{m_p} \tag{18}$$

$$I_p \frac{d\vec{\omega}_p}{dt} = \vec{T} \tag{19}$$

where I_p is the angular moment of inertia of the particle. These equations can be solved analytically to obtain the cartesian components of the particle velocity

$$V_x = U_x + (U_x - V_{x0})\exp\left(-\frac{\Delta t}{\tau_p} - \frac{3}{4}\frac{\rho}{\rho_p}\tau_p\right)\left(1 - \exp\left(-\frac{\Delta t}{\tau_p}\right)\right)$$

$$\left[\frac{F_{S_x} + F_{AM_x}}{m_p} + g\left(1 - \frac{\rho}{\rho_p}\right) + (V_z - U_z)\,\omega_{p_y} + \frac{1}{2}\left(\frac{\partial U_x}{\partial z} - \frac{\partial U_z}{\partial x}\right)\right]$$

$$(V_y - U_y)\,\omega_{p_z} + \frac{1}{2}\left(\frac{\partial V_y}{\partial x} - \frac{\partial V_x}{\partial y}\right) \tag{20}$$

$$V_y = U_y + (U_y - V_{y0})\exp\left(-\frac{\Delta t}{\tau_p} - \frac{3}{4}\frac{\rho}{\rho_p}\tau_p\right)\left(1 - \exp\left(-\frac{\Delta t}{\tau_p}\right)\right)$$

$$\left[\frac{F_{S_y} + F_{AM_y}}{m_p} + (V_x - U_x)\,\omega_{p_z} + \frac{1}{2}\left(\frac{\partial U_y}{\partial x} - \frac{\partial U_x}{\partial y}\right)\right]$$

$$(V_z - U_z)\,\omega_{p_x} + \frac{1}{2}\left(\frac{\partial V_z}{\partial y} - \frac{\partial V_y}{\partial z}\right) \tag{21}$$

$$V_z = U_z + (U_z - V_{z0})\exp\left(-\frac{\Delta t}{\tau_p} - \frac{3}{4}\frac{\rho}{\rho_p}\tau_p\right)\left(1 - \exp\left(-\frac{\Delta t}{\tau_p}\right)\right)$$

$$\left[\frac{F_{S_z} + F_{AM_z}}{m_p} + (V_y - U_y)\,\omega_{p_x} + \frac{1}{2}\left(\frac{\partial U_z}{\partial y} - \frac{\partial U_y}{\partial z}\right)\right]$$

$$(V_x - U_x)\,\omega_{p_x} + \frac{1}{2}\left(\frac{\partial V_x}{\partial z} - \frac{\partial V_z}{\partial x}\right) \tag{22}$$

70

Subscript 0 denotes the value at the beginning of the time subinterval Δt. The quantity τ_p is the hydrodynamic particle response time defined as

$$\tau_p = \frac{d_p^2 \rho_p}{18 f_{\text{corr}} \mu} \tag{23}$$

For the angular velocity we have

$$\vec{\omega}_p = \frac{1}{2} \vec{U} + \left(\omega_{p0} - \frac{1}{2} \vec{U}_0 \right) \exp\left(-\frac{60\mu}{\rho_p d_p^2} \Delta t \right) \tag{24}$$

The last forces to be considered are those by particle-wall and particle-particle collisions acting as impulses. The importance of the latter depends on the frequency of the collisions. The mutual interaction of particles must be taken into account in cases of high particle-to-fluid volume load ratio. There are criterions for determining when this is necessary [22, 23]. Briefly, it can be said that, for the regimes considered in this work, the load ratios were far below those which would demand particle-particle collision modelling.

For particle-wall collisions a model of a sphere hitting a smooth wall was developed. For the particular problem of modeling of particle motion in high temperature regimes, due to the fact that particles which hit the wall melt instantaneously, this model was not used. Instead, it was assumed that all particles which hit the wall stick on it as evaporating droplets.

By LSD model the instantaneous gas velocity components in the equation of particle motion were treated as stochastic parameters and calculated as a sum of mean velocity component and velocity fluctuation. Fluctuation in every direction was computed as a product of local turbulence intensity in that direction and independently generated random number with Gaussian distribution. Isotropic turbulence field was assumed $u_i' = (2k/3)^{1/2}$. The instantaneous fluid velocity components are kept constant during the time interval equal to the Lagrangian integral time scale $T_L = 5k/12\varepsilon$, which corresponds to the lifetime of biggest eddies. The effective eddy size was also assumed to be isotropic, *i. e.* $L_L = T_L (2K/3)^{1/2}$. The model takes into account the motion of particle relative to the eddy, *i. e.* the effects of crossed trajectories for larger and more inert particles. This gives the possibility to stop the eddy-particle interaction and start generating the new eddy after the end of the previous eddy lifetime or when particle leaves the eddy.

Model of heat and mass transfer between phases

A particle injected in plasma flow is heated, melted and evaporated. Its temperature computation is based on both heat and mass transfer between plasma and itself. Total heat transfer is the sum of convective and radiative heat transfer rates:

$$Q_{\text{conv}} + Q_R = \pi \text{Nu} \bar{\lambda}_g d_p (T_g - T_p) + \frac{4}{9} \pi k_{ap} d_p^2 (F_x + F_r) - \frac{8}{9} \pi k_{ap} d_p^2 \sigma T_p^4 \tag{25}$$

71

Here, Nu is the Nusselt number for convective heat transfer, $\overline{\lambda}_g$ is thermal conductivity of pure plasma computed for the mean plasma-vapor temperature in the particle boundary layer, k_{ap} is coefficient of absorption of the particle surface, d_p is the instantaneous particle diameter. The equation for particle heating and evaporation (sublimation) is:

$$Q_p \quad m_p c_p \frac{dT_p}{d\tau} \quad H_v \mathrm{Sh} \rho_g D_v \pi d_p (X_v \quad X_{vp})$$

(26)

where c_p is the specific heat of particle material, H_v is the latent heat of evaporation (sublimation). Sh is the Sherwood number for convective mass transfer, D_v is coefficient of diffusion of vapor in plasma, X_v and X_{vp} are mass fractions of vapor in plasma-vapor mixture outside the particle boundary layer and at particle surface, respectively. Assuming that partial pressure of vapor at the particle surface equals the saturation pressure p_{vs} at the particle temperature and p_b is the absolute gas pressure within the plasma reactor, mass fraction of the vapor at the particle surface is calculated as:

$$X_{vp} \quad \frac{1}{1 \quad \dfrac{M_g}{M_v} \quad \dfrac{p_b}{p_{vs}} \quad 1}$$

(27)

Here, M_g and M_v are molecular mass values of plasma and solid phase, respectively.

As a balance of the two energy rates one obtains the equation for particle temperature:

$$\frac{dT_p}{d\tau} \quad \frac{\pi \mathrm{Nu} \overline{\lambda}_g d_p}{m_p c_p} (T_g \quad T_p) \quad \frac{H_v}{m_p c_p} \mathrm{Sh} \rho_g D_v \pi d_p (X_v \quad X_{vp})$$
$$\frac{4}{9} \frac{\pi k_{ap} d_p^2}{m_p c_p} (F_x \quad F_r) \quad \frac{8}{9} \frac{\pi k_{ap} d_p^2 \sigma T_p^4}{m_p c_p}$$

(28)

Presence of T_p^4 makes the numerical solution rather difficult. Therefore, linearization has been performed ($T_p^4 \quad a \quad bT_p$) i. e. the fourth power temperature dependence has been approximated by a linear regression in small temperature interval in which the particle temperature lies in the considered instant of time. Introducing the abbreviations:

$$\alpha \quad \frac{m_p c_p}{\pi \mathrm{Nu} \overline{\lambda}_g d_p}$$

$$\beta \quad \frac{8}{9} \frac{\pi k_{ap} d_p^2 \sigma T_p^4}{m_p c_p}$$

$$\chi \quad \frac{H_v \dfrac{dm_p}{d\tau} \quad \dfrac{4}{9} \pi k_{ap} d_p^2 (F_x \quad F_r)}{m_p c_p}$$

and assuming them constant in the short time interval $\Delta\tau$, the exact solution for particle temperature is:

$$T_p = T_{p0} \exp\left(-b\beta \frac{1}{\alpha}\Delta\tau\right) + \exp\left(-b\beta \frac{1}{\alpha}\Delta\tau\right)\left[1 - \frac{a\beta\left(\frac{T_g}{\alpha} - \chi\right)}{b\beta\frac{1}{\alpha}}\right] \quad (29)$$

where T_{p0} represents the particle temperature at the beginning of that short time period.

During the period of melting there is no change of particle temperature. From an equation analog to eq. (28) one can calculate the mass of the particle m_{ps} in the solid state:

$$m_{ps} = m_{ps0} - [\pi\mathrm{Nu}\bar{\lambda}_g d_p(T_g - T_p) + H_v\mathrm{Sh}\rho_g D_v\pi d_p(X_v - X_{vp}) + \frac{4}{9}\pi k_{ap}d_p^2(F_x - F_r) - \frac{8}{9}\pi k_{ap}d_p^2\rho T_p^4]\frac{\Delta\tau}{H_f} \quad (30)$$

where H_f is the latent heat of melting and m_{ps0} is mass of the particle in the solid state at the beginning of the short time period.

Nusselt and Sherwood number used in the above equations were calculated from Ranz-Marshall relations, modified for the high temperature conditions:

$$\mathrm{Nu} = \frac{qd_p}{(S_\infty - S_s)} = (2 + 0.6\mathrm{Re}^{1/2}\mathrm{Pr}^{1/3})f(1 + B)^{-0.7} \quad (31)$$

where Nu is the Nusselt number, q the specific heat flux, d_p, the particle diameter,

$$S_\infty = \int_{300}^{T_\infty} k(T)dT \quad \text{and} \quad S_s = \int_{300}^{T_s} k(T)dT$$

the heat conduction potentials at the free stream plasma temperature T_∞ (same as T_g – gas temperature), and particle surface temperature T_s (same as T_p – particle temperature), respectively, $k(T)$[W/m/K] the thermal conductivity function of temperature, Re the Reynolds number based on the particle diameter and relative speed between the particle and the plasma, Pr is the Prandtl number. For the calculations of Reynolds and Prandtl numbers, integral mean values of plasma properties in the boundary layer surrounding the particle *i. e.* in the range from T_s, to T_∞ were used, due to high temperature difference $\Delta T = T_\infty - T_s$.

Correction factor to heat transfer f, due to noncontinuum *i. e. Knudsen effect*, is based on the theoretical predictions for the "temperature jump" (slip flow) regime (0.001 < Kn < 0.1 or even up to Kn* ≤ 0.8), modified for the thermal plasma conditions:

$$f = \frac{S_\infty - S_g}{S_\infty - S_s} = \left[1 + \frac{2 - \Theta_h}{\Theta_h}\frac{\chi}{1+\chi}\frac{4}{\mathrm{Pr}_s}\mathrm{Kn}^*\right]^{-1} \quad (32)$$

where Θ_h is thermal accommodation coefficient (a value $\Theta_h = 0.9$ is used in calculations), χ the specific heat ratio at T_s, Pr_s the Prandtl number at T_s, and Kn^* the effective Knudsen number defined as: $\mathrm{Kn}^* = 2\mathrm{Pr}_s(S_g - S_s)(H_g - H_s)/(\rho_s v_s d_p)$; H_g and H_s being the specific enthalpy of gas at "jump" temperature T_g and T_s respectively, ρ_s the plasma density at T_s, and v_s, [m/s] the mean molecular speed which can be calculated from the kinetic theory relation: $v_s = 2(2RT_s/\pi)^{0.5}$ where R J/kg/K is the perfect gas constant. The value of the "jump" heat conduction potential S_g corresponding to T_g in the vicinity of particle surface, is calculated by iteration from equation above. Correction factor B takes into account the influence of the particle evaporation on heat transfer and drag coefficient: $B = (H_g - H_s)(1 + q_r/q_{con.})/H_v$, where q_r and $q_{con.}$ are the radiative and convective heat fluxes to particle and H_v the latent heat of evaporation.

The drag coefficient C_D involved in the equation of particle motion was estimated by using the following relationships: for $\mathrm{Re} < 0.2$, $C_D = 24/\mathrm{Re}$ (based on Stokes' equation), for $0.2 \le \mathrm{Re} < 2$, $C_D = 24/\mathrm{Re}(1 + 3\,\mathrm{Re}/16)$ (Oseen equation), while for $2 \le \mathrm{Re} < 21$, $C_D = 24/\mathrm{Re}(1 + 0.11\mathrm{Re}^{0.81})$ and $C_D = 24/\mathrm{Re}(1 + 0.189\mathrm{Re}^{0.632})$ for $21 \le$ $\le \mathrm{Re} < 200$, are based on the experimental data confirmed by the numerical computations. The particle Reynolds number in these relations is calculated as previously defined. Corrections of the particle drag coefficient due to evaporation and noncontinuum effects were also included, based on previously defined parameters f and B:

$$C_D^{\mathrm{cor}} \quad \frac{C_D f^{0.45}}{1 \quad B} \tag{33}$$

The correlation for mass transfer between particle and plasma, used in the model, is based on an analogy between mass and heat transfer:

$$\mathrm{Sh} \quad \frac{q_m d_p}{C_\infty \overline{D_v}(Y_\infty \quad Y_s)} \quad (2 \quad 0.6\mathrm{Re}^{1/2}\mathrm{Sc}^{1/3})f_m \tag{34}$$

where Sh is the Sherwood number, q_m the silicon mass flux between particle and plasma, C_∞ the total gas concentration in the free plasma stream, Y_∞ and Y_s, are the mole fraction of silicon vapor out of boundary layer and on the particle surface $\mathrm{Sc} \quad v/\overline{D_v}$, is the Schmidt number (ratio of integral mean values of kinematic viscosity and molecular diffusivity in the particle's boundary layer). The integral mean value of molecular diffusivity is defined by:

$$\overline{D_v} \quad \frac{S_\infty \quad S_s}{C_\infty} \quad {}^{T_\infty}_{T_s}\frac{k(T)dT}{C(T)D_v(T)} \quad {}^{1} \quad \frac{S_\infty \quad S_s}{C_\infty}(Z_\infty \quad Z_s) \quad {}^{1} \tag{35}$$

where Z_∞ and Z_s [J/mol] are the Z-potentials defined as integral of the ratio of thermal conductivity *v.s.* product of total gas concentration and molecular diffusivity functions in

74

the range from reference temperature $T_r = 300$ K to T_∞ and T_s respectively. Correction factor f_m, due to noncontinuum effects, is calculated (for the "jump" regime) by the relationship:

$$f_m = f \frac{Z_\infty - Z_s}{Z_\infty - Z_g} \left[1 + 2 \frac{2 - \Theta_m}{\Theta_m} \frac{Kn^*}{Sc^*} \right]^{-1} \tag{36}$$

where Θ_m is the mass accommodation coefficient (a value $\Theta_m = 0.8$ is used), Z_g is the Z-potential at T_g, and the modified Schmidt number Sc^* defined as: $Sc^* = [(S_g - S_s)/(S_\infty - S_g)][(Z_\infty - Z_g)/(H_g - H_s)]Pr_s/M$ where M being the molecular mass of the gas.

Particle size distribution and notion of the parcel

Since the sizes of solid particles and bubbles play an important role in their motion, their size distribution is also included in the model. Sommerfeld [24] showed that the log-Gaussian distribution for the particle size yields the best agreement of numerical results with experiment:

$$f(D_p) = \frac{1}{\sqrt{\pi s^2}} \exp \left[-\frac{\left(\ln \frac{d_p}{d_{pm}} \right)^2}{2s^2} \right] \qquad s^2 = \ln \frac{d_{pm}}{d_{pN\,max}} \tag{37}$$

In this equation, d_{pm} and d_{pNmax} are the mean and the most probable particle sizes, respectively. The standard deviation s is the width of the size distribution in the ensemble of particles. In this work it was assumed that $s^2 = 0.25$.

The Lagrangian approach can follow only a moderate number of particles. The real number of particles in the flow domain, however, is very large. For this reason, the special term "parcel" of particles was defined. Parcels represent a large bulk of particles with the same size, mass, velocity and position. The model is arranged such that every parcel represents the same mass of a disperse phase. This means that different parcels in general represent different numbers of real particles, depending on the parcel (particle) size. Thus, the distribution of the parcel size differs from the particle size distribution. In order to represent the particle size distribution (eq. 37) in the flow field, the parcel size distribution has to be as follows

$$g(d_p) = \frac{\pi d_p^2 \rho}{3 m_p \sqrt{2\pi s^2}} \exp \left[-\frac{\left(\ln \frac{d_p}{d_{pm}} \right)^2}{2s^2} \right] \tag{38}$$

Numerical results

Axisymmetric reactor is schematically shown in fig.1. High temperature nitrogen plasma flow enters the vertical chamber of radius R and length L, through the central inlet of radius r_{in} at the top of the reactor. The secondary fluid flow laden with solid particles at room temperature is injected from the same side through the conical annular channel with inlet radii r_1 and r_2 and angle α. The products can leave the reactor through a central opening of radius r_{ex} at the reactor bottom. All reactor surfaces are shielded with uncooled high temperature material and all dimensions (L, R) refer to the inside surfaces of the shield.

(a)

(b)
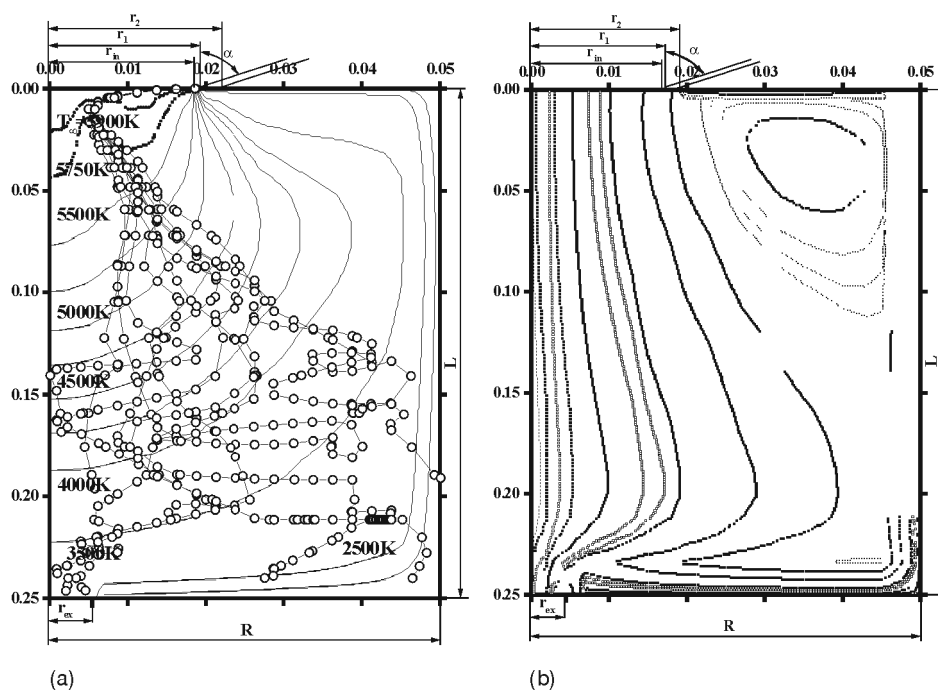
Figure 1. Axial section of the reactor with computed curves of constant: (a) plasma temperature with some particles trajectories, and (b) stream function for the example with following parameters: $r_1 = r_{in} = 18.75$ mm, $r_2 = 21.75$ mm, $R = 50$ mm, $L = 250$ mm, $r_{ex} = 6.25$ mm, $T_w = 1500$ K, $T_{w,bottom} = 1700$ K; nitrogen flow: $m_{in} = 2.07$ g/s, $\varphi_{pl} = 30°$, $T_{in} = 6000$ K, $m_{sec} = 0.24$ g/s; silicon powder: $m_{Si} = 0.127$ g/s, $d_{po} = 40$ ìm, $\alpha = 87.5°$

Numerical analysis of interphase momentum, heat and mass transfer thermal plasma flows

Computer simulation, analysis of the obtained numerical results and conclusions will be explained through an example with the following values of reactor parameters [25]: inlet plasma channel radius $r_1 = r_{in} = 18.75$ mm, outer radius of injection channel $r_2 = 21.75$ mm, reactor radius $R = 50$ mm, reactor length $L = 240$ mm, radius of exit channel $r_{ex} = 6.25$ mm, temperature of the shield $T_w = 1500$ K, $T_{w,bottom} = 1700$ K, nitrogen plasma flow $m_{in} = 2.07$ g/s, angle correlating tangential (swirl) W_{in} and axial U_{in} plasma velocity component ($W_{in} = U_{in} \mathrm{tg}\varphi_{pl}$) $\varphi_{pl} = 30^o$, inlet plasma temperature $T_{in} = 6000$ K, secondary nitrogen mass flow rate $m_{sec} = 0.24$ g/s, silicon powder mass flow $m_{Si} = 0.127$ g/s, initial diameter of Si particles $d_{po} = 40$ ìm, angle of injection channel $= 87.5^o$. Axial and radial component of the particle inlet velocity and its starting position in the exit section of the injection channel were treated as a stochastic parameters, which means that they have random values with Gaussian distribution around mean values defined by mass flow rate of secondary gas and geometric parameters of the channel. For this example, in fig. 1 were shown the calculated curves of constant: (a) plasma temperature T_∞ with some particles trajectories, and (b) stream function in the axial section of the reactor. Practically in the whole reactor there exist two different radial zones: central region ($r < r_2$) of high axial plasma velocity and high temperature and wide peripheral region ($r_2 < r < R$) of low plasma velocities ($U < 10$ m/s) and lower temperature with recirculating flow near the top of the cylindrical wall. Particles are injected practically radially in the boundary layer between these two zones so they can penetrate into the high temperature, high viscous plasma core.

Calculated trajectories of some particles in axial cross section of the reactor presented in fig. 1a, show effective particle penetration into the central high tempera-ture plasma flow, due to the good optimization of particle injection parameters, which is important problem in practice due to high sensitivity of few parameters. With expansion of turbulent plasma flow, particles are widely spread from the central region and for $x > 0.1$ m they are present in a whole cross section.

Analysis of the Reynolds number (for the particles with trajectories shown in fig. 1(a) given in fig. 2, shows that flow regime around the particle is highly viscous ($Re_p < 1$) due to the high viscosity of nitrogen plasma. Namely, at the beginning, injected particles have negative radial velocity while plasma
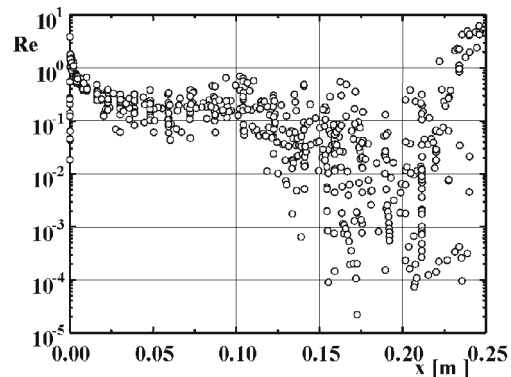
Figure 2. The particle Reynolds number as a function of its axial position in the reactor

77

flows axially and, due to high relative speed, Re_p number can be up to 3. Along the trajectory, up to $x < 0.05$ m relative velocity decreases much faster than plasma viscosity in boundary layer surrounding particle, and as a result Re_p decreases very fast. In the middle part of the reactor relative velocity is small, particles strictly follow the plasma flow but still there is high discrepancy of Re_p number due to the turbulent plasma flow and high discrepancy of T_∞. In this example, the value $r_{ex} = 6.25$ mm is small, and plasma near the exit is accelerated up to the velocity of 185 m/s. As a result Re_p for Si particles present near the exit my be up to 10.

Computed particle temperature and plasma temperature (along trajectories shown in fig. 1a) as a function of axial particle position in the reactor are shown in fig. 3.
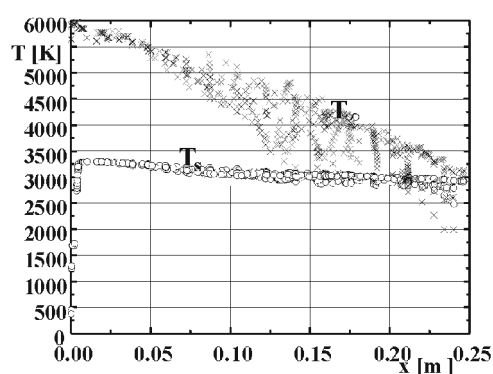
Figure 3. Particles temperature T_s and plasma temperature T_∞ as a function of particle axial position in the reactor

Taking into account the high boiling temperature of silicon ($T_B = 3513$ K at $p = 1$ bar) and the high equilibrium (gas--liquid) temperature [24], ($T_{eq} \approx 2850$ K) of Si for the analyzed example (with Si mass fraction in the system: 0.052) we can conclude from fig. 1a and 3 that plasma temperature in the whole reactor, except in the wall boundary layer, is higher than T_{eq} which enables an intensive interphase heat transfer and evaporation of particles. Radial gradients of the plasma temperature in the reactor are much higher than axial gradients (fig. 1a). Therefore, the plasma temperature along the trajectory, and in the same manner heat flux to the particle, will decay faster or slower depending on particle trajectory, as indicated in fig. 3 by high discrepancy of T_∞ for $x > 0.05$ m. The history of the particle temperature T_s along its motion indicates that heating and melting of particles is fast and is completed during the particle penetration into the central plasma region. This is due to the high temperature difference ($\Delta T = T_\infty - T_s > 3000$ K). After reaching the maximum value, near the center and at the beginning of the reactor, particle temperature decays very slowly. High discrepancy of the plasma temperature along the particles trajectory has relatively small influence on particle temperature if ΔT is high (for $x < 0.1$ m). Moreover, temperature of particles along their trajectories is always lower than T_B, indicating that the critical mechanism for particle evaporation is not mass transfer from the particle to the plasma, but heat transfer from plasma to the particle, even for large temperature difference of few thousands degrees in the first part of the reactor (fig. 3). The results presented in fig. 3 shows that high temperature gradients are present in the particle boundary layer along the whole trajectory, which indicates the necessity of dealing with integral mean values of plasma properties, as it was done.

In the case of the particle evaporation the flow field in the particle boundary layer is changed, which has influence on the drag coefficient, *i. e.* on the interphase momentum transfer. The heat transfer to the particle is decreased due to the heating of vapor in the boundary layer on the particle surface (heating from the particle temperature up to the plasma temperature). Correction factor *B* to the particle momentum and heat transfer due to evaporation, for the same particles as in fig. 1a, calculated along their trajectories, is shown in fig. 4. Factor *B* is important when the temperature difference ΔT is high, *i. e.* at the beginning of the trajectory. But as particle
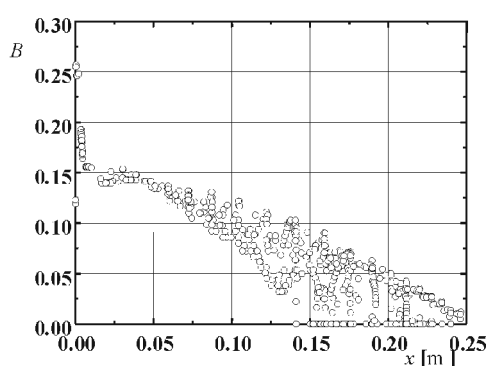
Figure 4. Correction factor *B* to momentum and heat transfer as a function of particle axial position in the reactor
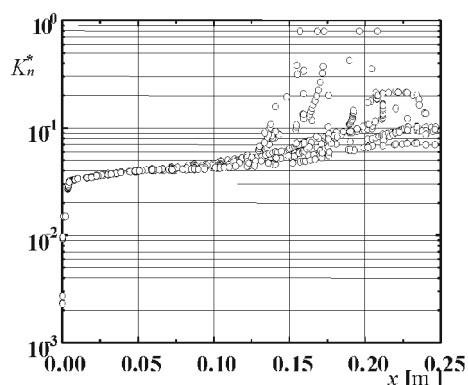
Figure 5. Particle effective Knudsen number as a function of its axial position in the reactor

is heated up very fast from 350 K to ~3300 K, value of *B* drops from 0.26 to 0.14 and corresponding correction of Nusselt number drops from –15% to –9%. As ΔT falls down along the trajectory the influence of the correction factor *B* is less important.

Computed values of the modified Knudsen number Kn* and the corresponding correction of the particle heat and momentum transfer *f* and mass transfer f_m, along particle trajectories 25 as in fig. 1a, are presented in fig. 5, 6, and 7, as functions of the particle axial position in the reactor. During the particle "injection" and "penetration" stage, while its diameter is constant, the value of Kn* rises from ~0.002 to ~0.03 (fig. 5), while the correction factors *f* and f_m drop from 1 to 0.87 (fig. 6 and 7) due to the increase of the particle temperature. Along the reac-
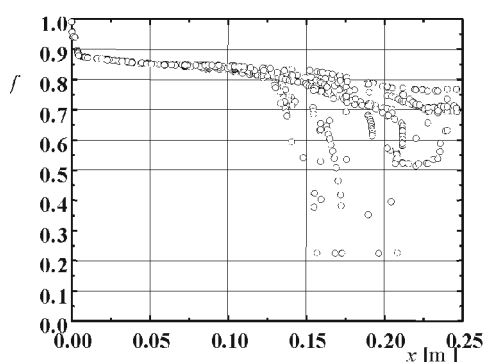
Figure 6. Correction factor *f* to momentum and heat transfer as a function of particle axial position in the reactor

79
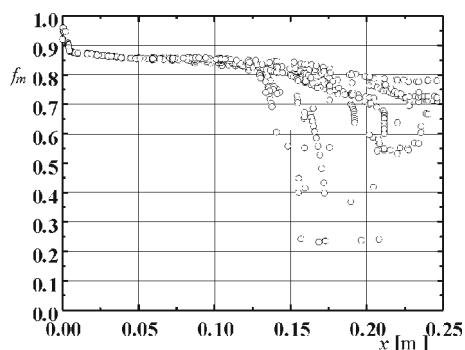
Figure 7. Correlation factor f_m to mass transfer as a function of particle axial position in the reactor

tor T_s decreases slowly but particle Knudsen number rises and correction factor f of the particle heat and momentum transfer decays constantly due to the particle diameter reduction, and for $d_p \sim 10$ µm Kn* ~ 0.1, $f \sim 0.7$ and $f_m \sim 0.7$. For such small particles heat transfer and evaporation will be still intensive if $\Delta T > 500$ K, in spite of Kn* intensive increase of and drop of f and f_m.

Particle Nusselt number, calculated 25 along the trajectories in fig. 1a, is shown in fig. 8 as a function of particle axial position in the reactor. For Nu = 2 the heat transfer to the particle is only by conduction, but in our case the particle evaporation is present, as well as noncontinuum effects, Nu can be less than 2. Heat transfer by convection, compared with conduction, drops from 32% at the beginning of the trajectory, to less than 15% after reaching the highest particle temperature level, due to high viscous flow around the particle, and changes very slightly along the trajectory except for the particles present near the exit of the reactor. From fig. 8 it is obvious that noncontinuum effects drastically reduce heat flux (Nu < 1.5) to small particles ($d_p < 10$ ìm).

The ratio of heat transfer to the particle by radiation *v. s.* conductive and convective heat transfer, calculated (for the particles with trajectories as shown in fig. 1(a) along their trajectories as a function of particle axial position in the reactor, is shown in fig. 9. Heat transfer to the particle by radiation is positive only during the short period

Figure 8. Particle Nusselt number as a function of particle axial position in the reactor
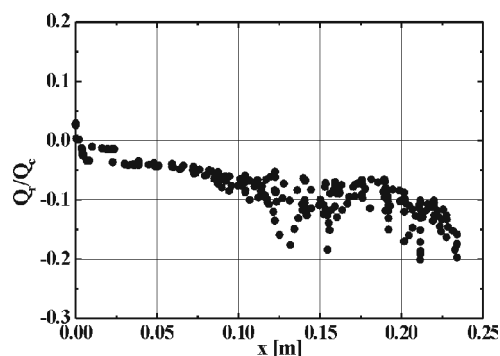
Figure 9. Ratio of heat fluxes to particle by radiation *v. s.* conduction and convection as a function of its axial position in the reactor

of particle heating up to the reactor wall (shield) temperature level, at the beginning of the trajectory (x < 0.01 m). As particle temperature rises, the heat lost by radiation increases and for the highest particle temperature level ($T_s \approx$ 3300 K, fig. 3) they are of the order 4% of the heat received by conduction and convection. Later, along the particle trajectory, as its temperature slowly falls down, the absolute value of heat lost by radiation decreases, but due to the high variations of T_∞ along the trajectory there are also a similar variations of the ratio Q_R/Q_c in the middle and in the second part of the reactor. For the particles present near or in the reactor wall boundary layer, where ΔT is small, the heat lost by radiation can be of the same level or higher than heat transferred by conduction and convection. When ΔT < 0, the ratio Q_R/Q_c is positive, indicating that heat is lost both by radiation and convection.

Particle diameter calculated along trajectories as in fig. 1a, as a function of residence time in the reactor is presented in fig. 10. The particles are heated up to the high temperature (fig. 3) very fast, in less than 1 ms, and after that the intensive evaporation begins. For the complete evaporation a much longer period is needed, $\Delta \tau$ = = 15-35 ms. The rate of particle diameter decrease is the highest in the first part of plasma reactor *i. e.* in the highest plasma temperature region due to the highest heat transfer rate to the particle. Later on along the trajectory, the decay of particle diameter is lower due to the smaller ΔT and decrease of heat transfer to the particle.

Presented analysis of momentum, heat and mass transfer between nitrogen thermal plasma (at atmospheric pressure) and injected Si particles in an axisymmetric shielded reactor, pointed out that the critical mechanism for particle evaporation is heat transfer to the particles. The main mechanism of interphase heat and mass transfer in these flow regimes is conduction and diffusion. The most efficient way to increase the quantity of heat transferred to the particles is to rise ΔT by increasing inlet plasma temperature, if possible up to 7000 K. In that case the heat transfer is increased not only by the temperature difference between plasma and particle, but also due to the increase of thermal conductivity of nitrogen plasma with the temperature up to or over 7000 K.

Correction to interphase momentum and heat transfer due to Si particle evaporation is important when the temperature difference between plasma and particle is high, and drops from 15% at the beginning of the trajectory (ΔT > 3000 K) to a few
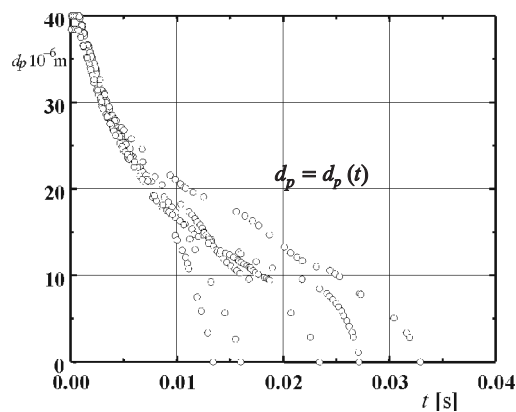

Figure 10. The calculated particle diameter along its trace as a function of particle residence period in the plasma reactor

81

(a)   (b)   (c)
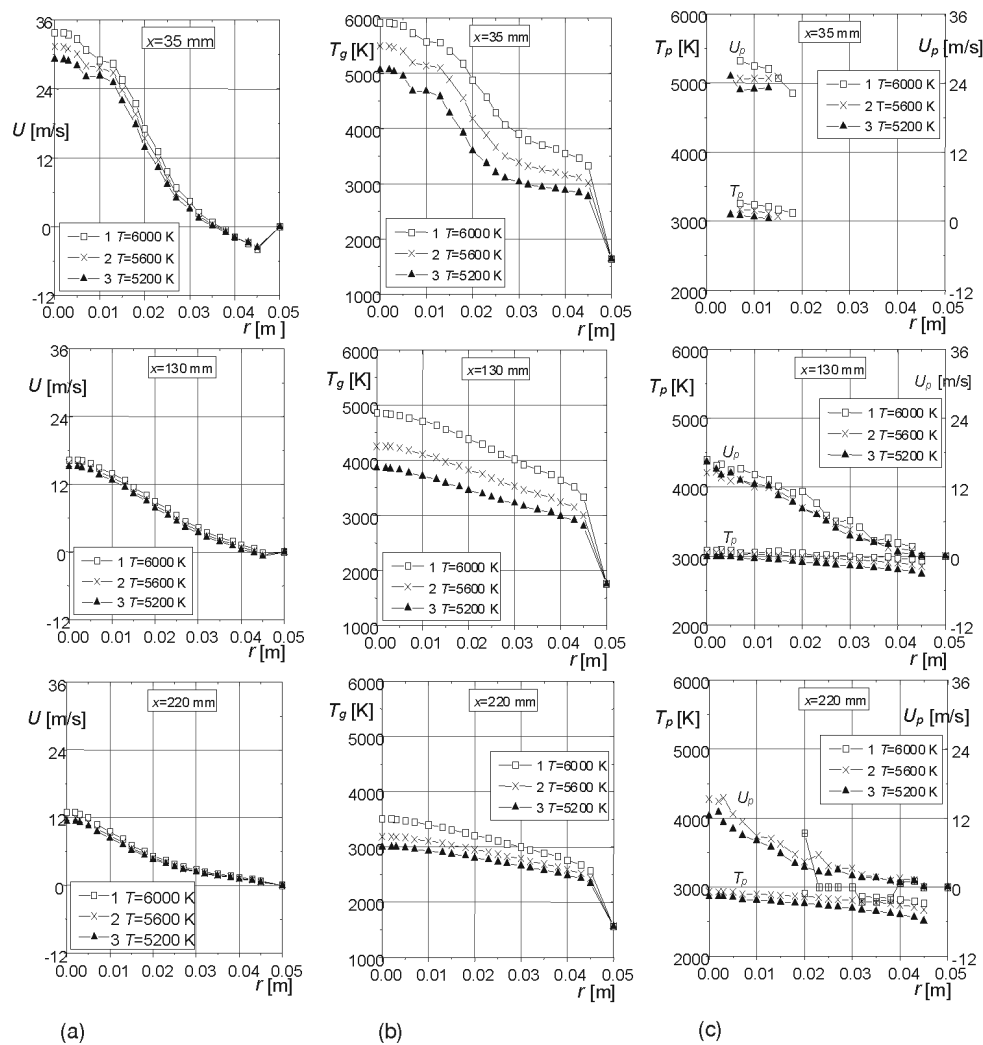
percents when $\Delta T \sim 500$ K. Corrections to momentum, heat and mass transfer due to noncontinuum effects are significant for small particles ($d_p < 50 \, \mu$m, especially for $d_p < 10 \, \mu$m) and have to be involved in the modeling of plasma particle evaporation processes.

For the presented example, computed results indicate that more than 97% of the injected mass of silicon powder have been evaporated, less than 0.08% left the reactor through the exit (as particles less than 10 μm in diameter), while the rest of injected silicon is "lost" on the reactor walls.

82
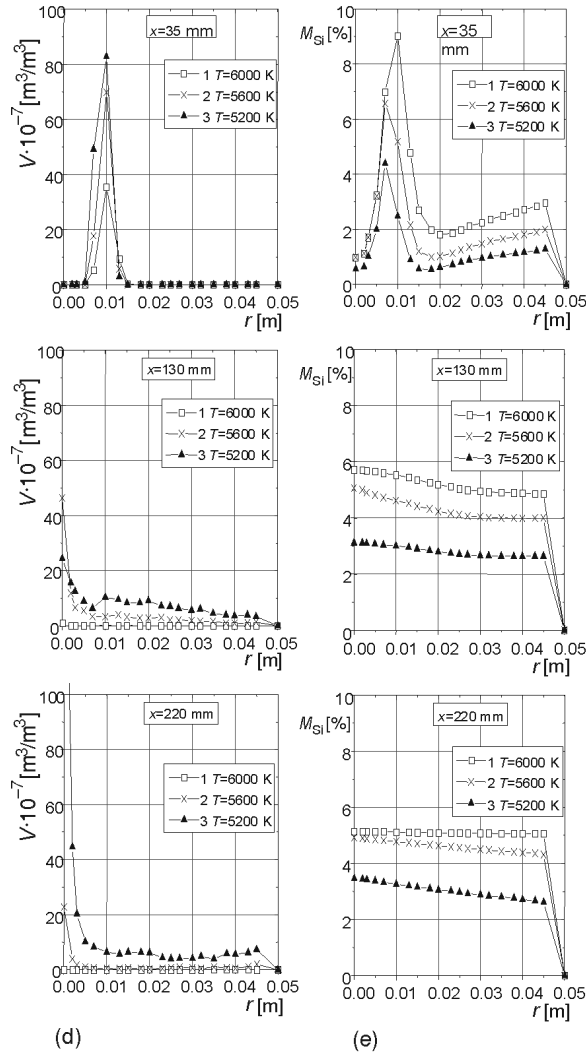
Figure 11. Computed radial profiles of:
(a) plasma velocity,
(b) plasma temperature, and
(c) average particle temperature and axial velocity,
(d) particle volume fraction, and
(e) mass fraction of silicon vapor, in three cross sections along the reactor
(x = 35, 130, and 220 mm)
illustrating influenc of inlet plasma temperature (curves No. 1 T = 6000 K; No. 2 T = 5600 K; No. 3 T = 5200 K on the evaporation process for the example with following values of other parameters:
$r_1 = r_{in}$ = 18,75 mm,
r_2 = 21.25 mm, R = 50 mm,
L = 240 mm, r_{ex} = 6.25 mm
T_w = 1500 K, $T_{w,bottom}$ = 1700 K; nitrogen plasma flow:
m_{in} = 2,07 g/s, φ_{pl} = 30°;
silicon powder flow:
m_{Si} = 0,127 g/s, d_{po} = 30 μm,
m_{sec} = 0,24 g/s, α = 87,5°

Influence of inlet conditions on particle evaporation efficiency in axisymmetric shielded plasma reactor

Computer simulation and numerical analysis has been conducted to show the influence of the following parameters on Si particle evaporation in thermal plasma flow reactor: 1 – inlet plasma temperature, 2 – inlet plasma velocity, 3 – particle initial diameter, 4 – particle injection angle α, and 5 – reactor wall temperature.

Influence of inlet plasma temperature is illustrated in fig. 11, 26, 27 . Here the following is presented: computed plasma gas velocity profiles (fig. 11a), plasma

temperature profiles (fig. 11b), particle mean axial velocity and temperature profiles (fig. 11c), particle volume fraction profiles (fig. 11d) and mass fraction of silicon vapor profiles (fig. 11e) in three cross sections at axial distances $x = 35$, 130, and 220 mm for three different inlet plasma temperature regimes: $1 - T_{in} = 6000$ K, $2 - T_{in} = 5600$ K, and $3 - T_{in} = 5200$ K, for the case of constant value of all other parameters as specified in fig. 11. Results in fig. 11a and fig. 11b show that inlet plasma temperature has minor influence on velocity field but great on temperature level in the whole reactor (fig. 11b curves 1, 2, and 3) and on interphase heat and mass transfer $i.$ $e.$ on evaporation process. Taking in mind high boiling temperature of Si ($T_B = 3513$ K at $p = 1$ bar) and high equilibrium (gas-liquid) temperature ($T_{eq} \approx 2850$ K 24) of silicon, we can conclude that for regime 1 plasma temperature in the whole reactor except in the wall boundary layer, is much higher than T_{eq} which enables an intensive interphase heat transfer and evaporation of particles. In other two regimes evaporation process is much slower due to smaller plasma temperature level compared with T_{eq} and in the peripheral region where $T_\infty < T_{eq}$ we can have even opposite process of condensation of silicon vapor on the particle surface. Particle volume fraction profiles (fig. 11d) and Si vapor mass fraction profiles (fig. 11e) prove faster evaporation with higher inlet plasma temperature and total evaporation in regime 1, much before the end of the reactor, while in other two regimes there are still liquid Si particles in the exit plasma flow (in regime with $T_{in} = 5200$ K, less than 60 mass% of injected silicon has been evaporated). Particle temperature profiles (fig. 11c) and data obtained along particle trajectory show that its temperature is always less then T_B, indicating that interphase heat transfer is critical for evaporation process. These examples shows great influence of inlet plasma temperature on evaporation process and the necessity to increase the value of T_{in} as much as possible, but at least over 5800 K in the case of evaporation of silicon particles in nitrogen plasma.

Influence of inlet plasma velocity 26, 27 on evaporation process is illustrated in fig. 12 where the following is presented: computed radial profiles of axial plasma velocity (fig. 12a), plasma temperature (fig. 12b), solid phase mean axial velocity and temperature (fig. 12c), solid phase volume fraction (fig. 12d), and mass fraction of silicon vapor profiles (fig. 12e) in three cross sections at axial distances $x = 35$, 130, and 220 mm for two regimes with different inlet plasma velocities obtained by changing the inlet radius: curves No. 1 $r_{in} = 18.75$ mm, $U_{in} = 33$ m/s; No. 2 $r_{in} = 13.75$ mm, $U_{in} = 61.3$ m/s. Other parameters common for both regimes are as specified in fig. 12. In regime 1 due to the higher inlet radius the central high temperature region of the reactor is wider while plasma velocity at the inlet and almost in the whole central region is approximately two times smaller than in the first regime. One can expect longer resident period of Si particles in the central, high temperature region and more efficient evaporation in regime 1. Plots in figs. 12d and 12e confirm these conclusions about inlet plasma velocity influence on evaporation process. Si particle volume concentration profiles indicate that in the regime with smaller inlet plasma velocity the evaporation process along the reactor is more efficient and at its end the total evaporation of Si particles with inlet diameter $d_{po} = 40$ µm is, while in regime 2 there are undesirable particles at the

reactor outlet. Higher mass fraction of silicon vapor in all three cross sections in fig. 12e in regime with lower inlet plasma velocity also illustrates difference in evaporation efficiency along the reactor and its superiority in comparison with regime 2. Results in fig. 12d show high particle concentration in the central, high temperature region, indicating good optimization of Si powder injection parameters, especially in regime 1, which is also necessary for efficient evaporation.

Influence of Si particle initial diameter 28, 3 on penetration, mixing and evaporation process is illustrated in fig. 13. Here, the following is presented: calculated instantaneous positions of some particles in axial section of the reactor, relative change of diameter d_p/d_{po} for the same particles along their trajectory as a function of its axial position in the reactor, and residence period as a function of particles axial position in the reactor, for four different initial Si particles diameters: (a) $d_{po} = 10\,\mu$m, (b) $d_{po} = 20\,\mu$m, (c) $d_{po} = 30\,\mu$m, and (d) $d_{po} = 40\,\mu$m. With the prescribed values of reactor working parameters, radial injection of finest Si powder ($d_{po} = 10\,\mu$m) results in its poor penetration into the central plasma flow region ($r \leq r_{\mathrm{in}}$). The highest concentration of particles is in the boundary layer between the central and the peripheral zone. Due to high turbulence intensity in boundary layer and quick rise of its thickness, particles with so small mass and momentum are quickly spread into low temperature recirculating flow. In spite of that, due to the high specific surface area of the powder, heat transfer is sufficiently high for complete evaporation of all particles at the beginning of the reactor ($x \leq 50$ mm) in less than 8 ms. Radial injection of coarser Si powder ($d_{po} = 20\,\mu$m) with the same mass flow rate and unchanged other parameters, results in better penetration and mixing with central high temperature plasma flow, due to the higher particle initial momentum. For the same reason, radial dispersion of Si particles in low temperature zone is slower. Higher heat transfer rate (compared with previous case, $d_{po} = 10\,\mu$m) due to the higher plasma temperature along particle trajectory, compensates lower specific surface of coarser Si powder. Therefore, the residence period up to complete evaporation is the same but axial length of particles trajectories is twice longer ($x \leq 100$ mm) due to the higher plasma velocity in the central region. With further increase of Si particle initial diameter, mass and momentum (figs. 13c and 13d), penetration into the high temperature plasma core is improved but dispersion of particles is lower, due to the higher plasma viscosity, lower turbulent intensity and higher particle mass. Intensive radial spread of Si particles with $d_{po} = 30\,\mu$m starts from $x \geq 50$ mm (fig. 13c) and for $d_{po} = 40\,\mu$m, from $x \geq 75$ mm. Due to the high plasma temperature and high heat flux rate along the trajectory, particles of $d_{po} = 30\,\mu$m can be completely evaporated at axial distances $x \geq 150$ mm and residence periods $\tau < 15$ ms. For the Si powder with lowest specific surface area, much longer ô and reactor length are needed for complete evaporation. In the case of analyzed conditions (fig. 13d, for Si particles with $d_{po} = 40\,\mu$m the residence period up to more than 40 ms are obtained), 96 mass% of the injected Si mass could be evaporated, while the rest is deposited on the reactor walls or escaped through the reactor exit as droplets.

Influence of conical injection channel angle α 3 on penetration, mixing and evaporation process is illustrated in fig. 14. Here, the following is presented: computed
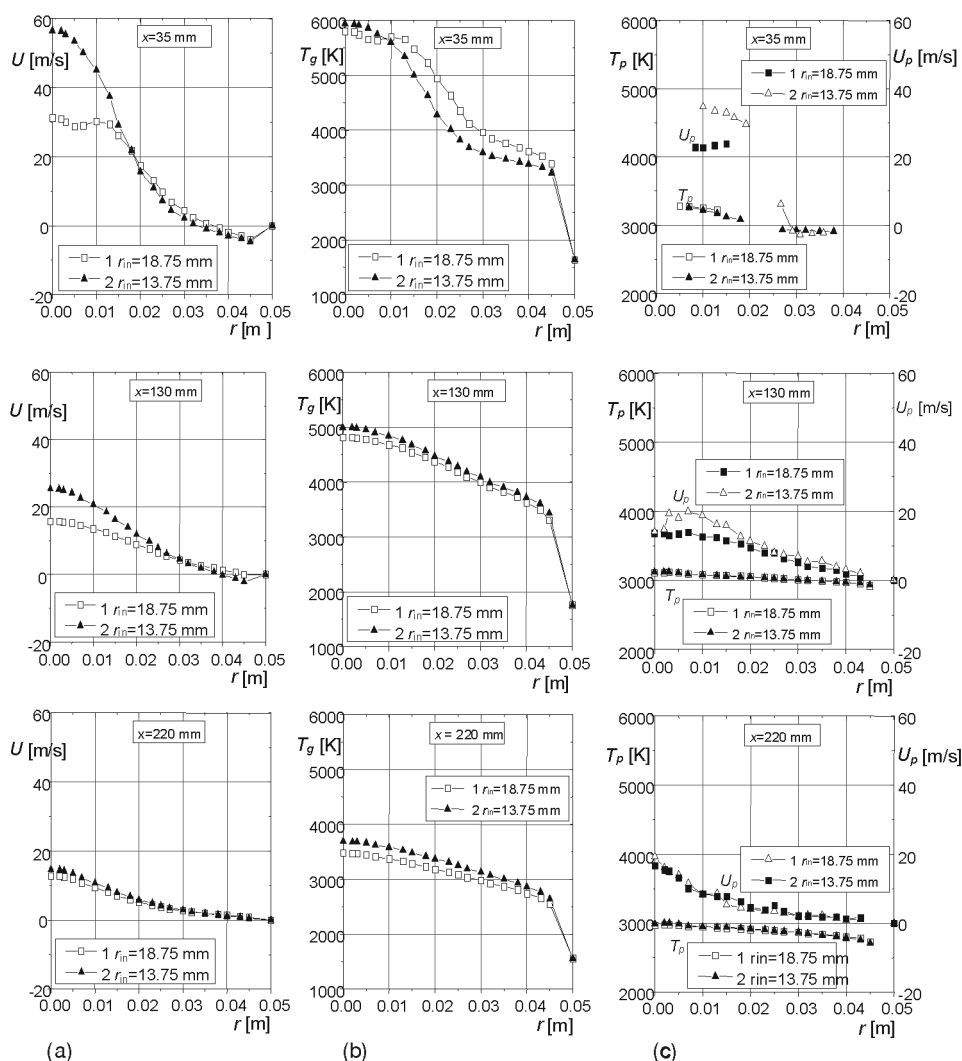
(a) instantaneous positions of some Si particles in axial section of the reactor, (b) plasma temperature T_∞ and particle temperature T_s along its trajectory, (c) change of particle diameter d_p along its trace, and (d) residence period, all as a function of particles axial position in the reactor, for three different values: $\alpha = 0°$, $\alpha = 60°$, and $\alpha = 90°$. Coaxial injection ($\alpha = 0°$) of Si particles ($d_{po} = 35$ μm) results in very poor penetration into the central plasma flow region. Particles are mostly concentrated in periphery recirculating zone (fig.14a, $\alpha = 0$) where plasma temperature is relatively low as well as the heat transfer rate to the particle, its temperature (fig. 14b) and evaporation rate i. e. particle diameter decrease (fig. 14c). Recirculating flow enables
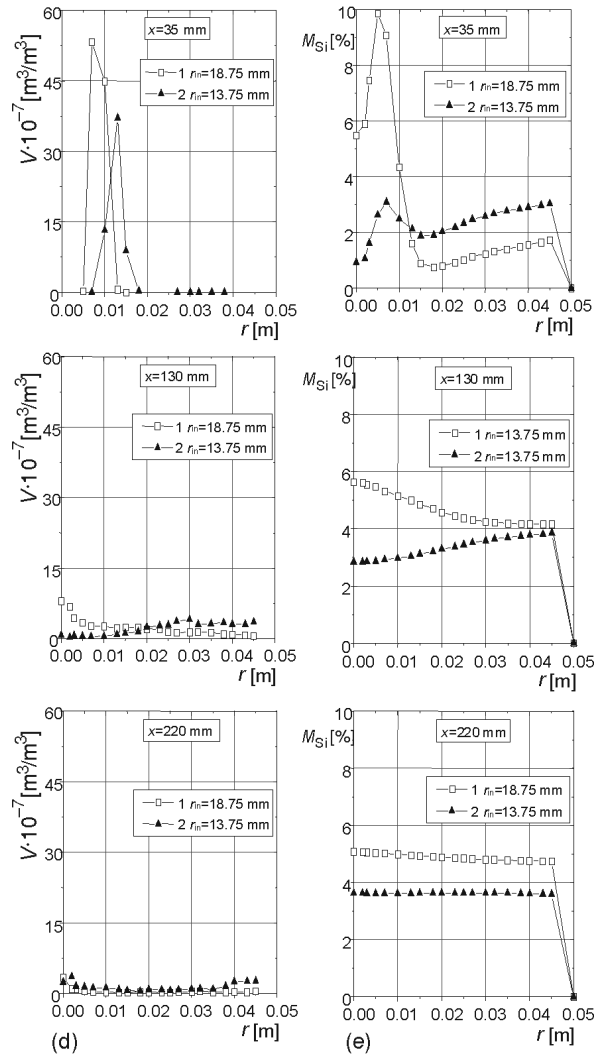
Figure 12, Computed radial profiles of:
(a) plasma velocity,
(b) plasma temperature, and
(c) average particle temperature and axial velocity,
(d) particle volume concentration, an
(e) mass fractin of silicon vapor in three cross sections along the reactor (x = 35, 130, and 220 mm) illustrating influence of inlet plasma velocity (curves, No. 1 r_{in} = 18.75 mm, U_{in} = 33 m/s;
No. 2 r_{in} = 13.75 mm
U_{in} = 61.3 m/s) on the evaporation process for the example with following values of other parameters:
r_1 = 18.75 mm, r_2 = 21.25 mm,
R = 50 mm,
r_{in} = 18.75 mm (U_{in} = 33 m/s)
r_{in} = 13.75 mm (U_{in} = 61.3 m/s
L = 240 mm, r_{ex} = 6.25 mm
T_w = 1500 K, $T_{w,bottom}$ = 1700 K;
nitrogen plasma flow:
T_{in} = 6000 K, m_{in} = 2,07 g/s,
φ_{pl} = 30;
Si powder flow:
m_{Si} = 0,127 g/s, d_{po} = 40 mm,
m_{sec} = 0,24 g/s, α = 87,5

high residence period but still, more than 50 mass% of injected Si mass has been deposited on reactor walls. For higher angle values (α = 60°, middle row diagrams) better penetration and mixing in the boundary layer of central plasma flow could be obtained. Plasma temperature in this region is higher, consequently the heat transfer rate and particle temperature is increased (fig. 14b, α = 60°), while residence period is decreased (fig. 14d). In the case of the radial Si powder injection (α = 90°, bottom row diagrams), the highest penetration into high temperature plasma core, highest heat flux rate and particle temperature level is obtained, resulting in the highest evaporation rate and complete evaporation of Si particles in the shortest period. In the case α = 60°,
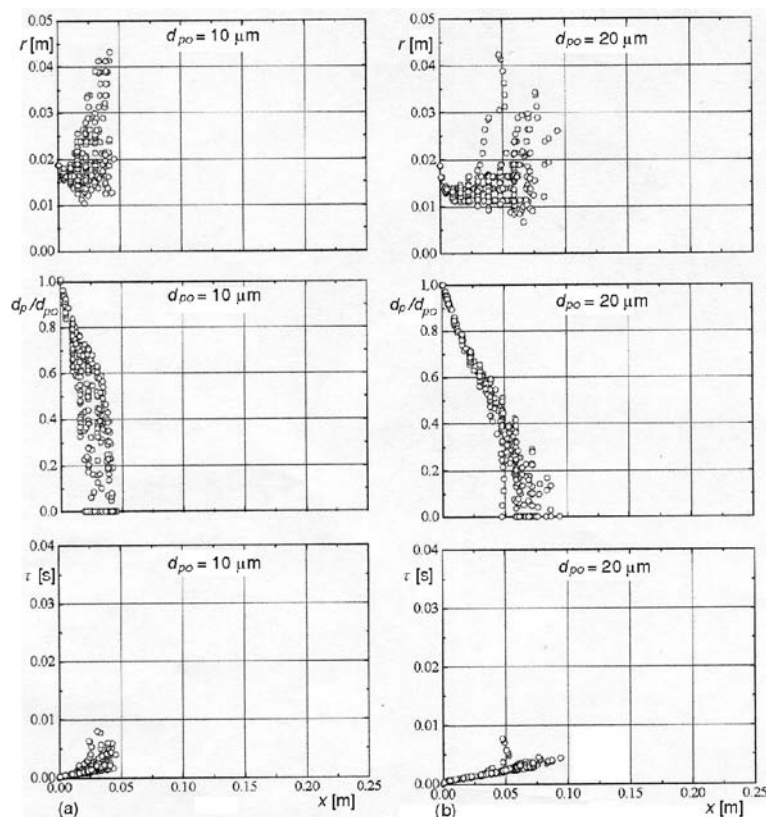
less than 30 mass% of injected Si mass is deposited on the reactor walls, while for $\alpha = 90°$ it is less than 1 mass%. In the case of radial Si powder injection, the increase of the injection velocity helps particle penetration into the high temperature plasma core and increases evaporation rate, but it must be carefully optimized.

Increase of reactor wall temperature in the investigated case of low particle concentration has minor direct positive influence, due to the lower heat losses from particle by radiation and indirect positive influence on evaporation process through the rise of plasma temperature level, due to the lower heat losses to the surrounding [29].

Evaporation efficiency for different particle materials
(Si, Al, Ti, B₂O₃)

Beside Si particles, the evaporation of some other starting solid precursors: Al, Ti, and B_2O_3 powders, that might be used for plasma synthesis of ultrafine nitride powders, was investigated. Results of numerical simulation for Al particles evaporation
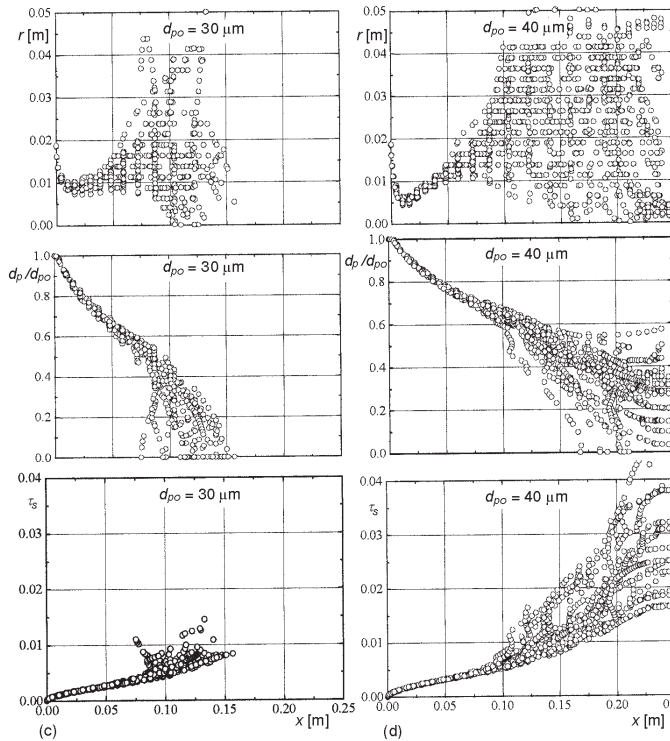
Figure 13. Computed instantaneous positions of some Si particles in axial section of the reactor, relative change of particle diameter d_p/d_{po} along its trace and particle residence period t all as function of particle axial position in the reactor, illustrating influence of particle initial dimaeter on mixing and evaporation process for the examples:
(a) $d_{po} = 10\,\mu$m,
(b) $d_{po} = 20\,\mu$m,
(c) $d_{po} = 30\,\mu$m, and
(d) $d_{po} = 40\,\mu$m, with following values of common parameters:
$r_1 = 18.75$ mm,
$r_2 = 21.25$ mm,
$R = 50$ mm,
$L = 240$ mm,
$r_{ex} = 6.25$ mm,
$T_w = 1500$ K,
$T_{w,bottom} = 1700$ K;
nitrogen plasma flow:
$T_{in} = 6000$ K,
$m_{in} = 2,07$ g/s, $\varphi_{pi} = 30°$;
Si powder flow:
$m_{Si} = 0.127$ g/s,
$m_{sec} = 0.24$ g/s, $\alpha = 87.5°$

in nitrogen plasma reactor 30 are presented in figs. 15 and 16. Compared with Si particles (fig. 1, $d_{po} = 40\,\mu$m) in almost the same reactor conditions and with the same evaporation efficiency it is possible that Al particles with higher initial diameter ($d_{po} = 50\,\mu$m) completely evaporate, due to the more appropriate thermophysical properties of aluminum [30]. Boiling temperature of Al ($T_B = 2798.7$ K at 1 bar) is much lower than for Si ($T_B = 3513$ K at 1 bar) *i. e.* aluminum has higher saturation pressure than silicon in the whole temperature range (fig. 17), which means higher evaporation efficiency of Al at lower temperatures. Also, the heat of sublimation (in the temperature range up to the melting point) and heat of evaporation of Al in the whole temperature range is much smaller compared with values for Si (fig. 18), which means higher evaporation rate (for the same heat transfer rate) of Al compared with Si. Still, Al particle temperature history along its trajectory (fig. 16) is lower than boiling temperature of aluminum, indicating that critical mechanism for particle evaporation is heat transfer to the particle, in spite of the increased temperature difference in the boundary layer surrounding Al particle compared with the case for silicon.

Titanium has lower heat of sublimation/evaporation compared with Al and Si (fig. 18), so that one could expect higher evaporation rate for the same heat transfer rate
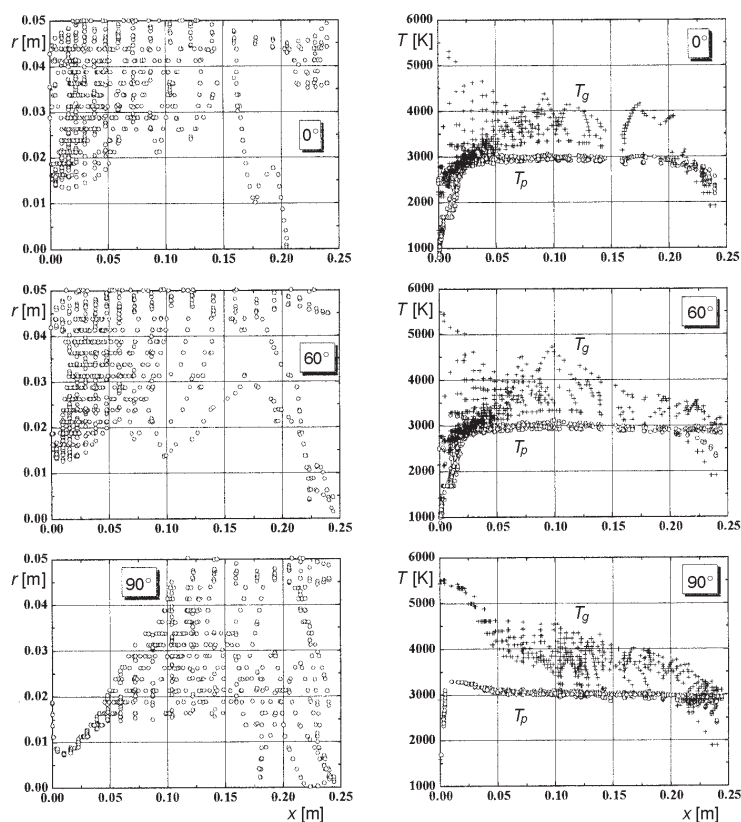
to the particles. But titanium has higher boiling temperature (T_B = 3688 K) and lower saturation pressure (fig. 17) in the whole temperature range compared with silicon. Due to these properties of titanium in almost the same plasma reactor conditions (fig. 19) and with the same evaporation efficiency, it is possible to evaporate Ti powder with smaller initial diameter (d_{po} = 30 μm) compared with silicon powder (d_{po} = 40 μm). Ti particle temperature level along its trajectory (fig. 20) is higher (due to the lower saturation pressure), but the temperature difference ΔT is almost the same for Ti and Si particles, in spite of the smaller heat transfer rate to Ti particles (due to the smaller ΔT).

Boron oxide has most suitable thermophysical properties for evaporation process between analyzed materials: low heat of sublimation/evaporation (fig. 18) and the highest saturation pressure (fig. 17) *i. e.* the lowest boiling temperature (T_B = = 2344.9 K at 1 bar). The results of the numerical simulations [31], presented in figs. 21 and 22, shows that boron oxide is almost easier to evaporate than Al powder. Still B_2O_3 particle temperature along its trajectory is lower than boiling temperature (fig. 22, $\Delta T >$ >65 K) indicating that critical mechanism for particle evaporation is heat transfer to the particle in spite of the increased temperature difference in the boundary layer
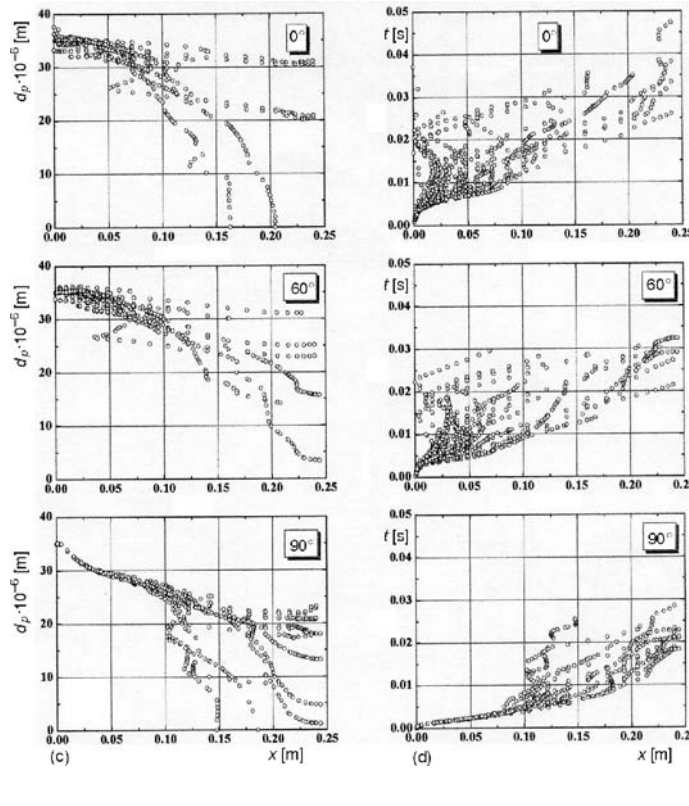
Figure 14. Computed: (a) the instanteneous position of some Si particles in axial section of the reactor, (b) particles temperature T_p and plasma temperature T_∞ (c) change of particle diameter d_p along tis trace, and (d) particle residence period, all as a function of particle axial postition in the reactor, ilustrating influence of injection angle ($\alpha = 0°$ top figures, $\alpha = 60°$ middle raw figures, and $\alpha = 90°$ bottom figures) on mixing and evaporation process for the example with following common values of other parameters: $r_1 = r_{\mathrm{in}} = 18.75$ mm, $r_2 = 21.25$ mm, $R = 50$ mm, $L = 240$ mm, $r_{\mathrm{ex}} = 6.25$ mm, $T_w = 1500$ K; nitrogen plasma flow: $T_{\mathrm{in}} = 6000$ K, $m_{\mathrm{in}} = 2.07$ g/s, $\varphi = 30°$, Si powder: $m_{\mathrm{Si}} = 0.1268$ g/s, $m_{N2} = 0.24$ g/s, $d_{po} = 35$ μm

surrounding B_2O_3 particle compared with the case for aluminum. The main reason is the increased value of the correction factor B to momentum and heat transfer due to the particle evaporation (fig. 23), compared to the usual range of values of B for the other three materials (fig. 4). Tem- perature dependence of boron oxide enthalpy [1] shows high increase of enthalpy in the range over 3000 K due to dissociation and over 4000 K due to ionization. Evaporated boron oxide has to be heated from particle temperature ($T_s \leq 2280$ K) to the surrounding plasma temperature (3500 K $< T_\infty < 6000$ K) and due to the high enthalpy increase of the boron oxide vapor in the particle boundary layer heat transfer to the particle is highly decreased, as indicated by the high values of the factor B (Nusselt number is decreased up to 76% for $B = 7$).

Evaporation efficiency in different plasma reactors configurations

Computer simulation was used to analyze the influence of plasma reactor configuration (axisymmetric multi torch system reactor with coaxial convergent plasma

Figure 16. Al particles temperature T_s and plasma temperature T_∞ as a function of particle axial position in the reactor
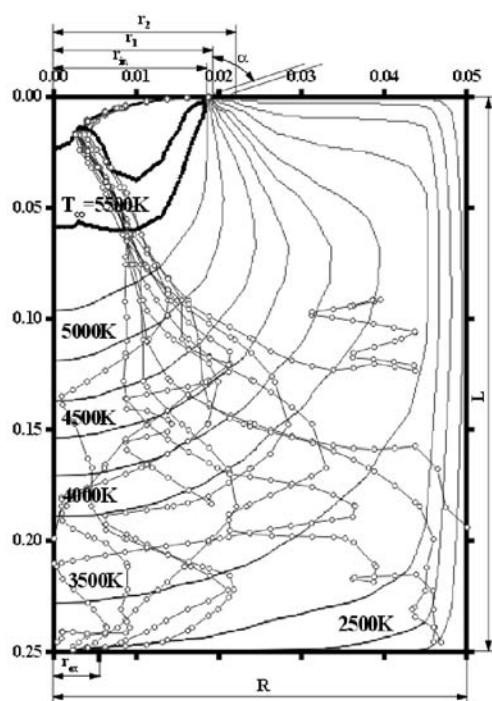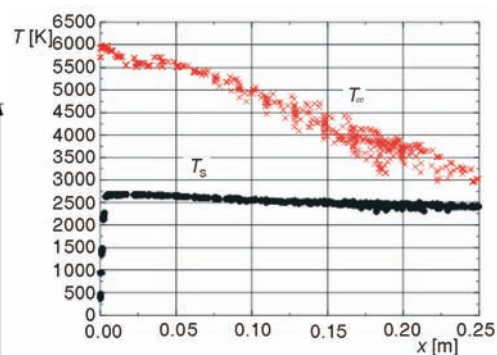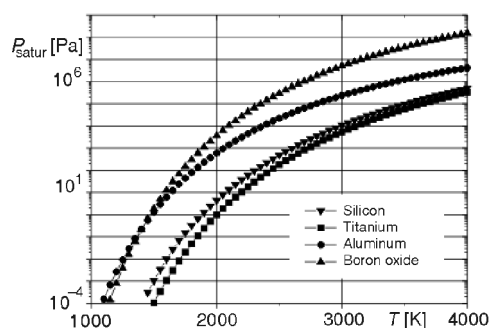

Figure 15. Axial section of the reactor with computed curves of constant plasma temperature and some Al particles trajectories for the example with following parameters
$r_1 = r_{in} = 18{,}75$ mm,
$r_2 = 21.25$ mm, $R = 50$ mm, $L = 250$ mm,
$r_{ex} = 6.25$ mm $T_w = 1500$ K, $T_{w\text{bottom}} = 1700$ K; nitrogen plasma flow: $T_{in} = 6000$ K, $m_{in} = 2{,}07$ g/s, $\varphi_{pl} = 30°$; Al powder: $m_{Al} = 0{,}127$ g/s, $d_{po} = 50$ ìm, $m_{sec} = 0{,}16$ g/s, $\alpha = 87{,}5°$

Figure 17. Temperature dependance of saturation pressure for Si, Al, Ti, and B_2O_3 [30]

flow and central flow of Si powder, versus classical axisymmetric plasma reactor with central plasma flow and radial injection of Si powder) on Si powder evaporation [32]. Mass flow rates and geometric parameters of the classical plasma reactor are as specified in fig. 24a and correspond to the experimental conditions for Si_3N_4 powder synthesis [4].

Mass flow rates, geometric and boundary conditions for the axisymmetric multi torch system reactor (fig. 24b) were set the same as for the classical reactor. Inlet mass axial velocities and temperature conditions are the same for both reactors, too.

Calculated results indicate that under investigated conditions the classical axisymmeteric plasma reactor is more suitable for Si powder evaporation compared with the multi torch system reactor, because:
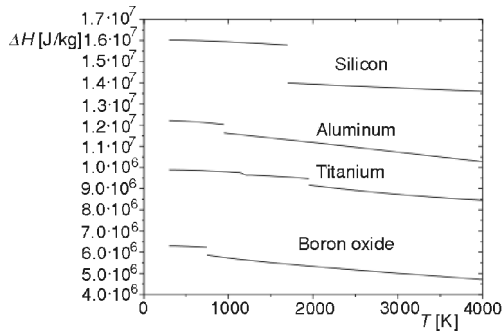
92

Figure 18. Temperature dependance of sublimation/evaporation heat for Si, Al, Ti, and B₂O₃ 30
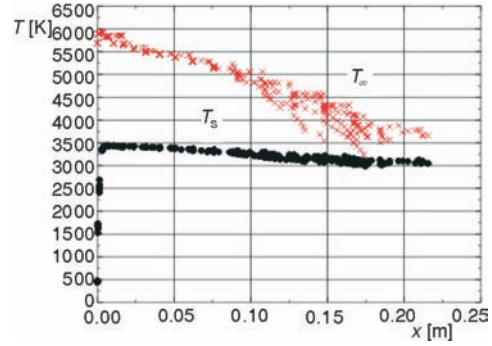

Figure 20. Ti particles temperature T_s, and plasma temperature T_∞ as a function of particle axial position in the reactor
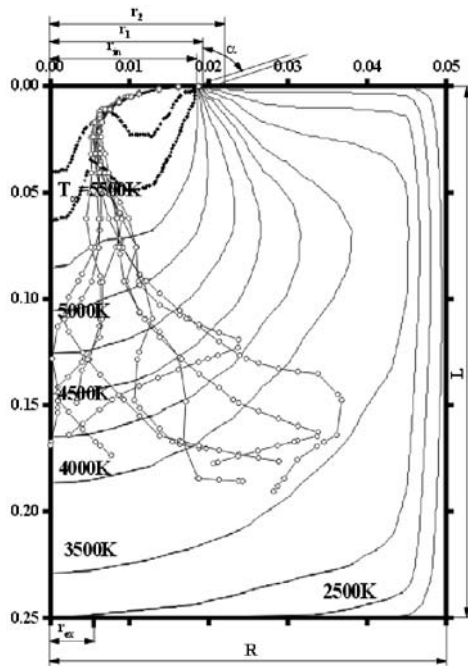

Figure 19. Axial section of the reactor with computed curves of constant plasma temperature and some Ti particles trajectories for the example with following parameters: $r_1 = r_{in} = 18{,}75$ mm, $r_2 = 21.25$ mm, $R = 50$ mm, $L = 250$ mm, $r_{ex} = 6.25$ mm, $T_w = 1500$ K, $T_{w,\text{bottom}} = 1700$ K; nitrogen plasma flow: $T_{in} = 6000$ K, $m_{in} = 2{,}07$ g/s, $\varphi_{pl} = 14°$; Ti powder: $m_{Ti} = 0{,}212$ g/s, $d_{po} = 30$ µm, $m_{\text{sec}} = 0{,}16$ g/s, $\alpha = 87{,}5°$
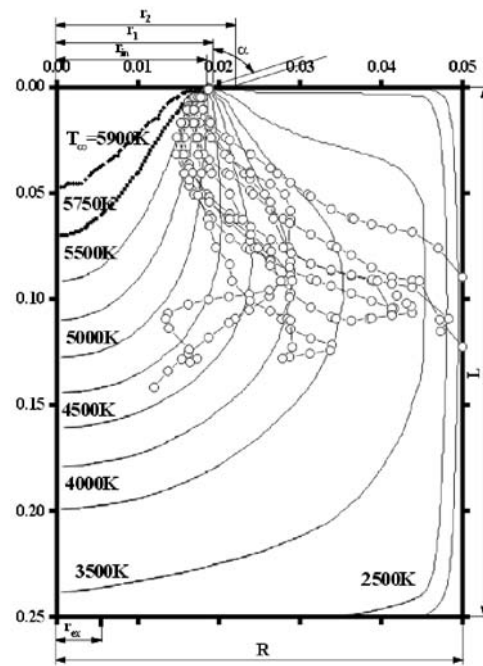

Figure 21. Axial section of the reactor with computed curves of constant plasma temperature and some B₂O₃ particles trajectories for the example with following parameters: $r_1 = r_{in} = 18{,}75$ mm, $r_2 = 21.25$ mm, $R = 50$ mm, $L = 250$ mm, $r_{ex} = 6.25$ mm $T_w = 1500$ K, $T_{w,\text{bottom}} = 1700$ K; nitrogen plasma flow: $T_{in} = 6000$ K, $m_{in} = 2{,}07$ g/s, $\varphi_{pl} = 14°$; B₂O₃ powder: $m_{B_2O_3} = 0{,}127$ g/s, $d_{po} = 50$ ìm, $m_{sec} = 0{,}16$ g/s, $á = 87{,}5°$
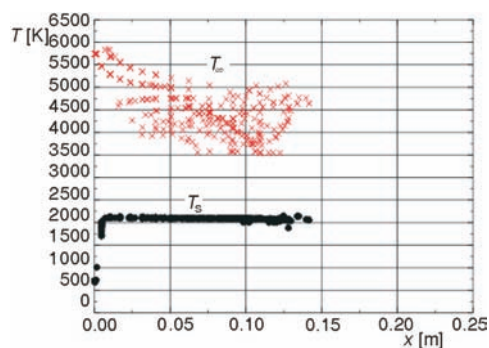
93

Figure 22. B$_2$O$_3$ particles temperature T_s and plasma temperature T_∞ as a function of particle axial position in the reactor
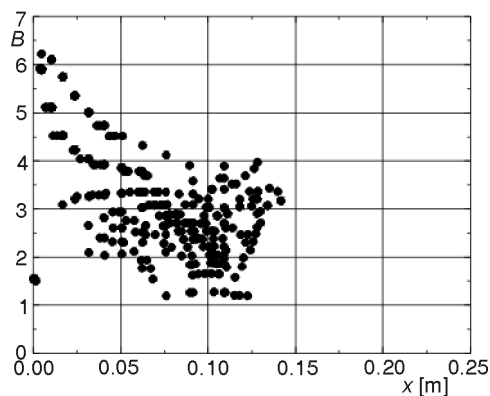
Figure 23. Correction factor B to mementum and heat transfer as a function of B$_2$O$_3$ particle axial position in the reactor
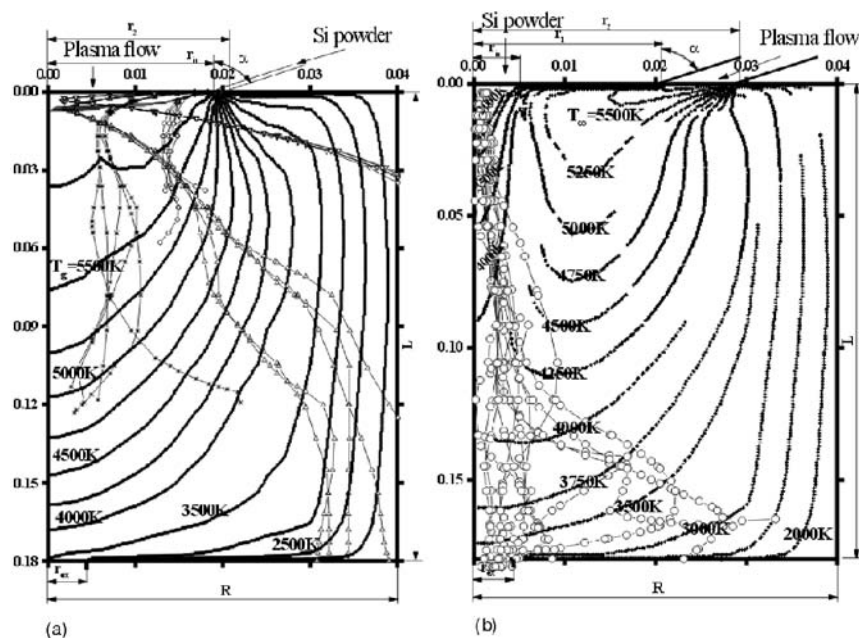

Figure 24. Axial section of (a) classical reactor, and (b) multi torch reactor with computed curves of constant plasma temperature with some particles trajectories (○ 10 μm; * 20 μm; △ – 30 μm; 45 μm) for the example with: (a) $r_1 = r_{in} = $ 19.5 mm, $r_2 = 20.5$ mm, $\alpha = 87.5°$ and (b) $r_{in} = 5$ mm, $r_1 = 21.5$ mm, $r_2 = 28.5$ mm, $\alpha = 60°$, and following values of common parameters $R = 40$ mm, $L = 180$ mm, $r_{ex} = 5$ mm, $T_w = 1500$ K, $T_{w,bottom} = 1700$ K; nitrogen flow: $m_{pl} = 4.5$ g/s, $T_{pl} = 5951$ K, $m_{N_2} = 0.29$ g/s; Si powder: $m_{Si} = 0.092$ g/s, d_{po} (10 μm 50 mass%; 20 μm 30 mass%; 30 μm 10 mass%; 45 μm 10 mass%)

94

– for the same inlet plasma temperature and the same plasma power, temperature level of plasma is much higher in classical reactor (fig. 24a), due to the much smaller convective heat losses to the top wall compared with the multi torch reactor configuration (fig. 24b),

– plasma temperature along the Si particles trajectory in the case of multi torch system reactor are rather small ($T \leq 4750$ K, fig. 24b) for intensive heat transfer to the particles; on the contrary, in the case of Si powder radial injection under optimal conditions into central plasma flow (fig. 24a) temperature of plasma along the Si particles trajectories is very high from the beginning, resulting in high heat transfer and intensive evaporation of silicon,

– in classical plasma reactor much higher evaporation efficiency is obtained for all four fractions ($d_{po} = 10\,\mu$m, 100 mass% evaporated; $d_{po} = 20$ ìm, 99.79 mass% evaporated; $d_{po} = 30\,\mu$m, 66.59 mass% evaporated; $d_{po} = 45\,\mu$m, 11.89 mass% evaporated); in the classical reactor under investigated conditions 87.8 mass% of the injected Si powder is evaporated, while in the multi torch system reactor only 61.2 mass%.

Acknowledgments

Nomenclature

C_D – drag coefficient, –
C_∞ – total gas concentration in the free plasma stream, kmol/m³
c_p – specific heat of particle material, J/kg/K
D_v – coefficient of diffusion of vapor in plasma, –
d_p – particle diameter, m
d_{pm} – mean particle size, m
$d_{pN\max}$ – the most probable particle size, m
d_{po} – initial diameter of Si particles, m
f – correction factor to heat transfer, –
f_m – correction factor due to noncontinuum effects, –
H_f – latent heat of melting, J/kg
H_g – specific enthalpy of gas at "jump" temperature T_g, J/kg
H_s – specific enthalpy of gas at "jump" temperature T_s, J/kg
H – latent heat of evaporation (sublimation), J/kg
h – enthalpy of gas mixture, J/kg
Kn*   – effective Knudsen number, –
k – turbulent kinetic energy, J
$k(T)$ – thermal conductivity, W/mK
k_{ap} – coefficient of absorption of the particle surface, –
L – vertical chamber length, m
M – molecular mass of gas, kg/mol
M_g – molecular mass values of plasma, kg/mol
M_v – molecular mass values of solid phase, kg/mol

m_{in} – nitrogen plasma flow, g/s
m_n – mass of a parcel, kg
m_p – particle mass, kg
m_{sec} – secondary nitrogen mass flow rate, g/s
m_{Si} – silicon powder mass flow, g/s
Nu   – Nusselt number for convective heat transfer, –
P – fluid pressure, Pa
Pr_s – Prandtl number at T_s, –
p_b – absolute gas pressure within the plasma reactor, Pa
p_{vs} – saturation pressure at the particle temperature, Pa
q – specific heat flux, W/m^2
q_{con} – convective heat flux to particle, W/m^2
q_m – silicon mass flux between particle and plasma, kmol/m^{2}s
q_r – radiative heat flux to particle, W/m^2
R – vertical chamber radius, m
Re   – Reynolds number, –
r_{ex} – central opening radius, m
r_{in} – central chamber inlet radius, m
r_1, r_2 – conical annular channel inlet radii, m
S_g – heat conduction potential at T_g, W/m
S_s – heat conduction potential at T_s, W/m
S_∞ – heat conduction potential at T_∞, W/m
Sc   – Schmidt number, –
Sh   – Sherwood number for convective mass transfer, –
T_g – local plasma gas mixture temperature, K
T_p – particle temperature, K
T_s – particle surface temperature (same as T_p), K
T_w – temperature of the reactor shield, K
T_∞ – free steam plasma temperature (same as T_g),
t_{tot} – total time period covered by the calculation, s
U_i – cartesian velocity components, m/s
V_{cv} – control volume, m^3
V_p – particle volume, m^3
X_v – mass fractions of vapor in plasma-vapor mixture outside the particle boundary layer, –
X_{vp} – mass fractions of vapor in plasma-vapor mixture at particle surface, –
x_i – cartesian co-ordinates, m
Y_s – mole fraction of silicon vapor on the particle surface, –
Y_∞ – mole fraction of silicon vapor out of boundary layer, –
Z_g – Z-potential calculated for the gas temperature, J/mol
Z_s – Z-potential calculated for the particle temperature, J/mol
Z_∞ – Z-potential calculated for the free plasma stream, J/mol

Greek leters

α – particle injection angle, °
Δt_{cv} – the total time of a parcel spent in the control volume, s
ε – turbulent dissipation rate, m^2/s^3
Θ_h – thermal accommodation coefficient, –
Θ_m – mass accommodation coefficient, –
λ_g – thermal conductivity of pure plasma, W/mK
μ – fluid dynamic viscosity, Pa·s

μ_t – turbulent viscosity, Pa·s
v_s – mean molecular speed, m/s
ρ – fluid density, kg/m³
ρ_s – the plasma density at T_s, kg/m³
τ_p – hydrodynamic particle response time, s
φ_{pl} – angle correlating tangential (swirl) and axial plasma velocity component

References

1 Kostić, Ž., Stefanović, P., Pavlović, P., Thermodynamic Consideration of B-O-C-H-N System for Boron Nitride Powder Production in Thermal Plasma, *Proceedings* (Ed. C. Galassi), 4th Euro Ceranics 1995, Gruppo Editoriale Faenza Editrice S.p.A., Italy, Vol. 1, pp. 307-314
2 Chang, Y., Young R., Pfender, E., Silicon Nitride Synthesis in an Atmospheric Pressure Convection-Stabilized Arc, Plasma Chem. and Plasma Process., *9* (1989), pp. 277-289
3 Pavlović, P., Kostić, Ž., Stefanović, P., Thermal Plasma Synthesis of Ultrafine Si₃N₄ and SiC Ceramic Powders, *Materials Science Forum*, 214, Transtec Publications Ltd., Switzerland, 1996, pp. 205-214
4 Stefanović, P., Pavlović, P., Kostić, Đ., Šikmanović, S., Cvetinović, D., Synthesis of Ultrafine Si₃N₄ Powder in a DC Thermal Plasma, *Proceedings*, ISPC-13, 18-22 August, 1997, Beijing, China, pp. 2084-2089
5 Mostafa, A. A., Elghobashi, S. E., A Two-Equation Turbulence Model for JET Flows Laden with Vaporising Droplets, *Int. J. Multiphase Flow*, *11* (1985), pp. 515-533
6 Migdal, D., Agosta, V. D., A Source Flow Model for Continuum Gas-Particle Flow, *Trans. ASME*, *34* (1967), pp. 860-865
7 Crowe, C. T., Sharma, M. P., Stock, D. E., The Particle-Source-in-Cell (PSI-CELL) Model for Gas-Droplet Flows, *J. Fluids Eng.*, *99* (1977), pp. 325-332
8 Rubinow, S. I, Keller, B., The Transverse Force on a Spinning Sphere Moving in a Viscous Fluid, *J. Fluid Mech., 11* (1961), pp. 447-459
9 Saffman, P. G., The Lift on a Small Sphere in a Shear Flow. *J Fluid Mech., 22*, (1965), pp. 385-400
10 Matsumoto, S., Saito, S., Monte Carlo Simulation of Horizontal Pneumatic Conveying Based on the Rough Wall Model, *J. Chem. Engng.*, ???*Japan*, *3* (1970), pp. 223-230
11 Tsuji, Y., Oshima, T., Morikawa, Y., Numerical Simulation of Pneumatical Conveying in a Horizontal Pipe, *KONA 3* (1985), pp. 38-51
12 Milojević, D., Lagrangian Stochastic-Deterministic (LSD) Prediction of Particle Dispersion in Turbulence, *Part. Part. Syst. Charact., 7* (1990), pp. 181-190
13 Sommerfeld, M., Žiković, G., Recent Advances in the Numerical Simulation of Pneumatic Conveying Through Pipe Systems, Computational Methods in Applied Science, ???*Invited Lectures and Special Technological Sessions of the First European Computational Fluid Dynamics Conference*, Brussels, 1992, pp. 201-212
14 Oesterle, B., Petitjean, A., Simulation of Particle-to-Particle Interaction in Gas-Solid Flows, *Int. J. Multiphase Flow*, *19* (1993), pp. 199-211
15 Durst, F., Milojević, D., Schönung, B., Eulerian and Lagrangian Predictions of Particulate Two-Phase Fflows: A Numerical Study, *Appl. Math. Modelling, 8* (1984)*, pp.101-115
16 Hinze, J. O., Turbulence, 2nd Edition, Mc-Graw-Hill, New York, 1975
17 Patankar, S. V., Numerical Heat Transfer and Fluid Flow, , Hemisphere Publ. Co, New York, 1980
18 Lee, S.L., Durst, F., On the Motion of Particles in Turbulent Duct Flows, *Int. J. Multiphase Flow*, *8* (1982), pp.125-146

19   Ahmad, K., Goulas, A., A Numerical Study of the Motion of a Single Particle in a Duct Flow, *Proceedings,* 5th International Conference Pneumatic Transport of Solids in Pipes, London, April 16-18, 1980, pp. 75-97

20   Durst, F., Raszillier, H., Analysis of Particle-Wall Interaction, *Chem. Eng. Sci.*, *44*, (1989), pp. 2872-2879

21   Matsumoto, S., Saito, S., On the Mechanism of Suspension of Particles in Horizontal Pneumatic Conveying: Monte Carlo Simulation Based on the Irregular Bouncing Model, *J. Chem. Engng., of Japan, 3* (1970), pp. 83-92

22   Živković, G., Mathematical Modelling of Two-Phase Gas-Particle Flow in Horizontal Tubes and Channels, *PhD Dissertation*, University of Belgrade, 1996

23   Crowe, C. T., On the Relative Importance of Particle-Particle Collisions in Gas-Particle Flows, *Proceedings,* Conf. Gas-Borne Part. (1981), paper C78/81 , pp. 135-137

24   Kostić, Ž., Stefanović, P., Pavlović, P., Thermodynamic Consideration of Si-N and Si-H-N Systems for Silicon Nitride Powder Production in Thermal Plasma, *Ceramic International*, *22* (1996), 3, pp. 179-186

25   Stefanović P., Pavlović P., Kostić Z., Oka S., Numerical Analysis of Momentum, Heat and Mass Transfer between Nitrogen Plasma and Injected Si Particles in Axisymmetric Reactor, *Heat and Mass Transfer under Plasma Conditions* (Ed. P. Fauchais), Begell House, New York, 1995, pp.169-176

26   Stefanović, P., Pavlović, P., Kostić, Ž., Numerical Analysis of Thermal Plasma Inlet Parameters Influence on Si Particle Evaporation in Axisymmetric Reactor, *Proceedings,* XVI Int. Symp. on the Phisics of Ionized Gases, Belgrade, 25-28 September, 1993, pp. 281-285

27   Stefanović, P., Pavlović, P., Kostić, Ž., Computer Simulation of Particle Evaporation in Thermal Plasma Flow Reactor, *Proceedings,* 21st Inter. Conf. on Phenomena in Ionized Gases, September 19-25, 1993, Bochum, Germany, Vol. 1, pp. 403-404

28   Stefanović, P., Pavlović, P., Kostić, Ž., Oka, S., Mathematical Analysis of Critical Parameters of Si Particles Evaporation in Axisymmetric DC Plasma Reactor, *Supp. au Journal of High Temp. Chem. Processes*, *1* (1992), 3, pp. 359-366

29   Stefanović, P., Pavlović, P., Kostić, Ž., Oka, S., Numerical Analysis of Heat Transfer between Nitrogen Plasma and Injected Si Particles in Axisymmetric Reactor, *Proceedings,* 10th International Conference on Heat Transfer, August 18-24, 1994, Brighton, England, Vol. 5, pp. 381-386

30   Glushko, V. P., Gurevich L.V., Thermodynamic characteristics of species (in Russian), Nauka, Moskva, T.I, (1978), T.II, (1979), T.III, (1981)

31   Stefanović, P., Cvetinović, D., Pavlović, P., Kostić, Ž., Numerical Analysis of Momentum, Heat and Mass Transfer between Nitrogen Plasma and Injected B_2O_3 Particles Injected in Axisymmetric Reactor, Proceedings (Eds. P. Fauchais, J. Amouroux) 5th International Thermal Plasma Processing Conference, St. Petersburg, Russia, July 13-16, 1998, Progress in Plasma Processing of Materials, Beggel House Inc., New York, 1999, pp. 209-217

32   Stefanović, P., Cvetinović, D., Pavlović, P., Kostić, Ž., Numerical Analysis of Si Powder Evaporation in Axisymmetric Reactor with Coaxial Convergent Nitrogen Plasma Flow, Proceedings (Eds. P. Fauchais, J. Amouroux), 5th International Thermal Plasma Processing Conference, St. Petersburg, Russia, July 13-16, 1998, Progress in Plasma Processing of Materials, Beggel House Inc., New York, 1995, pp. 927-933

Authors' address:

P. Stefanović, D. Cvetinović, G. Živković,
S. Oka, P. Pavlović

"VINČA" Institute of Nuclear Sciences
Laboratory for Thermal Engineering and Energy
P. O. Box 522, 11000 Belgrade, Serbia and Montenegro

Corresponding author (D. Cvetinović):
E-mail: deki@vin.bg.ac.yu